



HYBRID MIXTURE THEORY-BASED MODELING OF UNSATURATED TRANSPORT IN A DEFORMING POROUS FOOD MATRIX DURING FRYING

Yash Shah , Pawan Singh Takhar* 

Department of Food Science and Human Nutrition, University of Illinois at Urbana-Champaign, Urbana, IL, USA

Correspondence to:

Pawan Singh Takhar at
ptakhar@illinois.edu;
Phone: +1 (217) 300-0486

*This author has
previously published as
Pawan P. Singh

How to Cite:

Shah, Y., & Takhar, P.
Hybrid mixture theory-
based modeling of
unsaturated transport in a
deforming porous food
matrix during frying.
InterPore Journal, 1(2),
ipj240824–6.
[https://doi.org/10.69631/
ipj.v1i2nr25](https://doi.org/10.69631/ipj.v1i2nr25)

RECEIVED: 14 Feb. 2024

ACCEPTED: 18 June 2024

PUBLISHED: 24 Aug. 2024

ABSTRACT

Physics-based modeling of deep fat frying is daunting given the intricacies involved in the transport of different phases (liquid water, gas, and oil) in a continuously deforming unsaturated porous matrix. To simplify model development, previous models for frying either ignored volume changes or used empirical relations. The model developed in this study solved the hybrid mixture theory-based unsaturated transport equations and mechanistically accounted for the volume changes of the porous food (potato) matrix. Pore pressure, the effective pressure on pore walls, was used as the driving force governing the volume changes. A good agreement was found between the model predictions and experimental results. The % mean absolute error for moisture content, oil content, and temperature is 5.57%, 22.42%, and 13.35%, respectively. Evaporation and gas expansion during frying led to high pressures in the porous matrix with a peak gauge pore pressure of approximately 19.16 kPa at the center of the sample. The high pressure restricted the frying oil from penetrating beyond the surface layers. Oil uptake mainly occurred during the early stages of frying ($t < 50$ s) when the pressure in the core was low, and towards the end of frying when the matrix was more susceptible to oil penetration because of decreasing pressure. The potato cylinder shrunk by 18.55% for a frying time of 300 s. The gauge pore pressure near the surface became negative, which led to the rapid contraction of the surface layers, and as a result, the porosity near the surface decreased. The average porosity was predicted to decrease by 5.06% after 300 s of frying. The evaporation zone expanded with frying time, and its peak progressively moved towards the core. The insights generated from the discussed mechanisms will guide the industry in optimizing frying techniques.

KEYWORDS

Unsaturated, Porous, Modeling, Deforming, Pressure, Temperature

This is an open access article published by InterPore under the terms of the Creative Commons Attribution-NonCommercial-NoDerivatives 4.0 International License (CC BY-NC-ND 4.0) (<https://creativecommons.org/licenses/by-nc-nd/4.0/>).



@2024 The Authors

1. INTRODUCTION

Deep fat frying is one of the most commonly used food processing operations. It involves completely immersing a food product in a high boiling point edible fat or oil, typically at temperatures between 150-190 °C, resulting in products that are widely appealing and consumed globally (14, 36). The portfolio of fried foods is diverse, including products such as chips, French fries, chicken nuggets, chicken patties, fish sticks, vegetable fritters, donuts, and even fried ice cream. The high frying temperatures and the presence of multiple phases (liquid water, gas, oil, and solid biopolymers) drive a wide range of chemical and physical changes, such as protein denaturation, starch gelatinization, retrogradation, glass transition, moisture evaporation, Maillard reaction, and caramelization (42, 135). These changes play a role in imparting the food with a unique color (golden brown), texture (crispy, dry crust with a moist core), and flavor.

Increasing caution has been practiced while consuming fried foods due to their high oil content, acrylamide accumulation, and toxic compound production during frying (14). Oil consumption has been linked to obesity and cardiovascular concerns (32, 62), and acrylamide has been identified as a potential carcinogen (104, 124). Thermo-oxidized compounds like polar and oligomer compounds, trans-fatty acids, and heterocyclic amines may be present in fried foods, adding to the health and safety-related concerns of fried foods (99, 133). These growing concerns have renewed the focus on optimizing existing frying techniques.

Similar to the physicochemical changes that make fried foods desirable, oil uptake and acrylamide accumulation depend on the complex interplay of various phenomena occurring during frying. Understanding and predicting the different transport mechanisms during frying could be the first step in finding ways to reduce oil uptake, or addressing more advanced problems, such as that of acrylamide accumulation.

There is extensive work available in the food literature on frying, including different types of experimental (7, 13, 27, 80, 81) and modeling (19, 35, 46, 88, 140) studies. However, given the complexities involved in frying, there remains significant scope for further improvement and advancement.

Purely experimental approaches can be time-consuming, expensive, and may generate limited insights. Mathematical models overcome these limitations; however, they require experimental data for estimating material properties and model validation. Experimental observations can also help refine a model by including or dropping specific terms in the equations. This strategy will be highlighted in this study.

Mathematical models for frying range from phenomenological or empirical models (15, 63, 127) to continuum-scale mechanistic models (18, 67, 68, 93). Further, processes like baking, microwaving, and frying involve evaporation. Previous models have described frying with either a sharp-moving vaporization front (59, 60), or with distributed evaporation in the porous matrix (18, 93). Datta (44, 45) and Halder et al. (67) discuss some of these models.

In recent years, there has been growing interest in the pore-scale modeling of foods (56, 74, 122, 131). Pore-scale modeling, however, is challenging for naturally occurring porous structures like food because of their complex pore geometries. The high computational costs limit the applicability of the models to smaller sample sizes or simplified geometries (74, 144). Additionally, microscale material properties are needed, which are difficult to measure and are not readily available in the literature. With advances in modeling techniques and computing power, pore-scale modeling offers promising prospects for future use. However, its practicality as a predictive tool is currently limited (123).

The current study uses a continuum-scale mechanistic model to study frying. Frying involves simultaneous mass and energy transfer coupled with microscopic and macroscopic changes in the food structure. Rapid heat transfer-driven water vaporization, moisture loss, and concomitant oil uptake in a porous biopolymeric matrix make frying an intricate unsaturated (pores not saturated with liquids but also containing gas/vapors) transport problem. Biopolymeric matrices like food have a hierarchy of

length scales and have the potential to shrink or swell, which further adds to the complexity of model development. A closer look at the multiscale nature of porous foods is provided in [Section 2.1](#).

Continuum-based porous media models for frying can be found in the works of Ni & Datta (93), Halder et al. (67, 68), Bansal et al. (17, 18), Sandhu and Takhar (108), and Takhar (120). The previous studies focused on modeling the heat and mass transfer during frying and were able to predict variables like moisture loss and temperature change with reasonable accuracy. However, there is room for improvement on three fronts. First, the previous models did not mechanistically account for the volume changes of the porous matrix during frying. Second, the predicted pressure during frying needs to be validated using pressure measurements. Third, the understanding of different oil uptake mechanisms is still incomplete, and there is a need to update previous models based on newer observations available in the literature.

Though volume change is viewed as a macroscopic quantity, there are accompanying spatial and temporal changes in porosity. Porosity is the space 'available' to the fluid phases to occupy within the porous structure. Changes in porosity are expected to affect the transport of the fluid phases (140). Additionally, a shrinking or swelling matrix represents a moving boundary problem, and the effect of this must be accounted for in the model and solution methodology. Ignoring volume changes may lead to significant disagreement between model predictions and experimental results (16). For example, Gulati et al. (65) showed that coupling volume change with the transport problem improved the agreement between measured and predicted temperatures for microwave drying of potato cubes.

Unlike saturated porous systems, where the change in volume of the matrix can be assumed to be equal to the loss of the liquid phase from the matrix (47), estimating volume changes for unsaturated systems is not straightforward. Vapor generation and gas expansion during frying cause the expansion of the matrix, whereas water loss causes shrinkage. As a result, there is more than one phenomenon causing volume change. Most previous frying models ignored volume changes of the porous matrix or, in some cases, empirically accounted (90, 140) for the volume changes. In this study, we accounted for the volume changes of the porous matrix mechanistically and used pore pressure as the driving force for these changes.

Pore pressure is the effective pressure applied on the pore walls by the phases occupying the pores. Many studies in the field of geological sciences have explored the relationship between pore pressure and deformation (89, 103, 109, 125, 139). However, its use for modeling volume change in porous food systems remains rare. An example of this can be found in the work of Ditudompo and Takhar (48), who modeled the transport mechanisms and expansion during the extrusion of starch. They used pore pressure as the key variable governing the expansion of the extrudate matrix. Further details about implementing this approach will be provided in [Section 2.5](#).

Unsaturated porous media models can predict the pressure changes during frying. However, in the previous frying models, a validation of the predicted pressures is unavailable (68, 108). The peak pressure predicted in some previous models was either much lower or much higher when compared to the data available in the literature. The measured peak gauge pressure in previous frying studies was of the order of 10 kPa (110, 135). The peak gauge pressure predicted by the models of Halder et al. (68) and Ni and Datta (93) was less than 2 kPa. On the other hand, the model developed by Sandhu and Takhar (108) predicted that the peak gauge pore pressure would be approximately 200 kPa. Therefore, there is a need for a model which can accurately predict the magnitude of pressure developed during frying. The impact of pressure development during frying on oil uptake and volume changes will be discussed in [Section 4](#).

1.1. Study Objectives

The study aims to closely highlight the transport mechanisms involved in frying, and by accounting for volume changes, we present an advancement of the previously published models. The model is validated using various measured variables detailed below. The focus is on generating insights into the underlying physics by analyzing the trends of the different model variables. This is further explored through

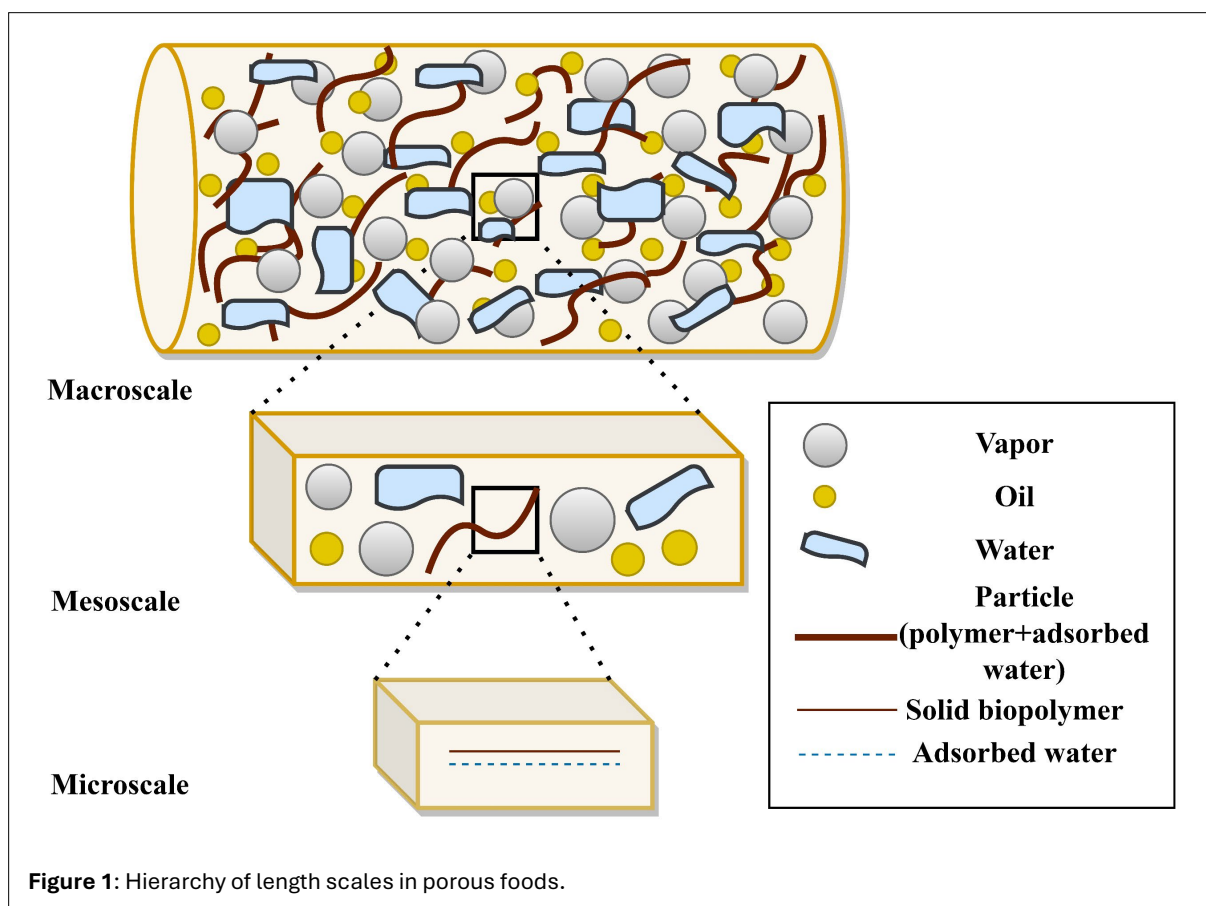
sensitivity tests on certain material properties. Additionally, we assess the model's limitations and present steps for future improvements.

The specific objectives of the study were: 1) to utilize a hybrid mixture theory (HMT)-based unsaturated transport model for conventional frying, 2) to mechanistically account for volume changes during frying, 3) to validate the model using measured data on moisture content, oil content, temperature, pressure, and volume changes, 4) to improve the understanding of transport mechanisms involved in the frying of a deforming material using simulation data generated with the validated model, and 5) to perform sensitivity tests on selected material properties

2. MATHEMATICAL MODEL DEVELOPMENT

2.1. Hierarchy of scales in biopolymeric matrices

Biopolymeric matrices, such as those found in foods, exhibit a hierarchy of length scales (130) (Fig. 1). At the microscale ($\sim 1 \mu\text{m}$), the solid biopolymers and the vicinal liquid (water) are seen distinctly (23). At the mesoscale ($< 10^3 \mu\text{m}$), the water-imbibed biopolymer is seen as an overlaying continuum of vicinal water and solid biopolymer, and a distinction between the two constituents cannot be made. Bulk phases like liquid water, oil, and vapors exist at the mesoscale as non-overlapping continua. At the macroscale ($> 10^3 \mu\text{m}$), there is a homogenization of all the bulk phases and water-imbibed biopolymers, forming a macroscale continuum.



Raw potatoes have a regular honeycomb-like arrangement of cells (134), held together by pectic substances that make up the outer layer (middle lamella) of the cell walls (40). The starch granules are present inside the cells. The overall tissue structure (parenchyma) in potatoes is made up of the cells and extracellular spaces occupied by fluid (liquid or gas) phases (40). In terms of length scales, the pores in

the cell membranes are at the microscale, the cell cytoplasm is at the mesoscale, and the tissue is at the macroscale (20).

Similar naturally occurring hierarchies are seen in soils (24, 57, 87) and other subsurface structures (149). However, the swelling and shrinking potential, along with the viscoelastic nature of foods, creates a more complex and interesting problem.

Phenomena occurring at lower scales often show up as mesoscale or macroscale changes (145). For example, the hydrophilic nature of solid particles causes water imbibition, leading to their swelling and subsequent deformation of the macroscopic matrix (21). This encourages the use of upscaling techniques. A range of upscaling techniques is available, and a description, along with the advantages and disadvantages of some of these techniques, can be found in Battiato et al. (20) and Cushman et al. (39).

2.2. Hybrid Mixture Theory

Whitaker's volume averaging method (138) and Hassanizadeh and Gray's HMT method (69, 70, 71) are two commonly used upscaling approaches. In the former technique, the mass, momentum, energy, and entropy balance equations, along with constitutive equations, are volume averaged to higher scales (mesoscale or macroscale). Though closed-form relations are obtained for the mesoscale counterparts of the microscale material properties, their experimental determination at the mesoscale is not straightforward (20, 21).

Hybrid mixture theory presents an alternate approach wherein only the field equations are upscaled. The constitutive theory is introduced at the higher scales, and the entropy inequality is utilized in the sense of Coleman and Noll (37). The advantage of this approach is that the material properties manifest at the macroscale, allowing them to be determined through relatively simpler macroscale experiments (20). A limitation of this approach is that the behavior of different material components (e.g., elastic solids, viscous liquids) is not modeled individually. Instead, their combined behavior is represented in a simplified form, such as viscoelasticity.

The HMT approach was originally developed by Hassanizadeh and Gray (69, 70, 71) for multiphase systems. While the earlier HMT works assumed a non-swelling porous medium, Achanta et al. (5) modified and extended the theory for swelling or shrinking systems by accounting for the interaction between the phases. A further extension was provided by Bennethum and Cushman (20, 22) by adding another scale (macroscale) to the problem. This requires the field equations to be averaged twice, from microscale to mesoscale and then from mesoscale to macroscale.

Previous HMT studies assumed the solid phase to be elastic and the liquid phase to be viscous at the microscale. At the macroscale, these microscale interactions resulted in viscoelastic behavior with short-memory effects (137). Microscale relaxation processes in a biopolymeric matrix, such as food, impact liquid transport through the matrix. However, this effect is overlooked when the solid phase is assumed to be purely elastic. Singh and colleagues (114, 115) extended the HMT approach by assuming the solid phase as viscoelastic at the microscale for two-scale and three-scale problems, respectively. The resulting theory was sufficiently general to model both Fickian and non-Fickian fluid transport, including the long-memory effects of polymers (114).

Many food processing operations, such as baking and frying, involve unsaturated transport and cannot be accurately modeled using saturated transport models. To address this, Takhar (120) developed HMT-based two-scale unsaturated transport equations specifically for biopolymeric systems.

This study utilizes Takhar's (120) HMT-based two-scale unsaturated transport equations for frying. The two-scale approach simplifies the three-scale approach by merging the micro and mesoscales, assuming a continuum for adsorbed and bulk fluid phases (145). The resulting scale can interchangeably be called the microscale or mesoscale. The field equations defined for this scale are upscaled to the macroscale, where the entropy inequality is invoked. The resulting system of equations is solved for macroscale

representative elementary volumes (REVs), which require less computational effort and fewer material property inputs compared to microscale or mesoscale domains, especially when computations are performed over the entire material.

Hybrid mixture theory-based models have been successfully applied to many food processes. They have been used to study saturated transport problems such as drying and sorption (1, 2, 96, 116, 117, 119, 121), as well as unsaturated transport problems like frying (18, 108), freezing (145), and extrusion (48).

2.3. Assumptions

Certain assumptions are made to reduce complexities in the model development. The liquid water, gas, oil, and solid phases are in a continuum. Gravitational forces are considered negligible for driving fluid flow compared to the other forces. The gas phase is an ideal mixture of water vapors and air. The solid and liquid phases are assumed incompressible at the microscale ($\rho^s = \rho^w = \rho^o = 0$), and the gas phase is assumed compressible ($\rho^g \neq 0$). The implication of this assumption will be seen when the mass balance equations for each phase are presented (Eq. 16, 17, 18 and 19). The overall matrix is still allowed to shrink or expand. This is possible because $\rho = \varepsilon^s \rho^s + \varepsilon^g \rho^g + \varepsilon^w \rho^w + \varepsilon^o \rho^o$, and changes in the volume fraction of the phases (ε^α , where $\alpha = s, g, w, o$) will change the density of the mixture even if individual phase densities (ρ^α) do not vary (30, 53). Further, we assume that there is a local thermal equilibrium between the phases, which allows us to use a single energy balance equation (common temperature) for the mixture of phases rather than individual energy balance equations for the phases (129). The temperature in the matrix can still vary spatially and temporally.

2.4. Field equations

2.4.1 Mass and Momentum Balance Equations

The fluid phases present in the pores are liquid water (w), oil (o), and gas (g). The gas phase is composed of water vapors (v) and air (a). The two-scale mass balance equation for a fluid phase α (where, $\alpha = w, o, g$) is given by Equation 1 (120):

$$\frac{D^s(\varepsilon^\alpha \rho^\alpha)}{Dt} + \nabla_{\mathbf{E}} \cdot (\varepsilon^\alpha \rho^\alpha \mathbf{v}^{\alpha,s}) - \frac{\varepsilon^\alpha}{\varepsilon^s} \dot{\varepsilon}^s \rho^\alpha = \sum_{\beta \neq \alpha} \beta \hat{\rho}^\alpha, \quad \text{where } \alpha, \beta = w, o, g \quad (1)$$

wherein the two-scale mass balance equation for the solid phase (Eq. 2) (120), was used to change the material time derivatives with respect to the α phase (D^α/Dt) to material time derivatives with respect to the solid phase (D^s/Dt).

$$\frac{D^s \varepsilon^s}{Dt} + \varepsilon^s (\nabla_{\mathbf{E}} \cdot \mathbf{v}^s) = 0 \quad (2)$$

The material time derivatives in the equations are also represented by a dot over the variables, for example, $\dot{\varepsilon}^s$. $\nabla_{\mathbf{E}}$ represents the gradient operator in Eulerian coordinates. ε^α , ρ^α and $\mathbf{v}^{\alpha,s}$ represent the volume fraction, density, and velocity of phase α with respect to the solid phase, respectively. The term on the RHS of Equation 1, $\beta \hat{\rho}^\alpha$, is the source/sink term that represents the mass transfer from the β phase to the α phase. The source/sink term couples the mass balance equations for different phases and ensures that mass is conserved. This term is characteristic of multiscale equations and is generally absent in single-scale equations (17). Evaporation changes liquid water to vapor, whereas condensation does the opposite. As a result, ${}^w \hat{\rho}^v = {}^w \hat{\rho}^g = -{}^g \hat{\rho}^w$. Since the oil phase does not exchange mass with other phases, ${}^w \hat{\rho}^o$ and ${}^g \hat{\rho}^o$ are equal to zero. Similarly, the solid phase does not exchange mass with the fluid phases (${}^\beta \hat{\rho}^s = 0$).

The generalized Darcy's law for the liquid phases is given by Equation 3 (120), where K^α , μ^α , p^α and, D^α are the permeability, dynamic viscosity, pressure, and diffusivity of phase α , respectively. B^α is the mixture viscosity of the biopolymeric matrix. The flow of phase α is governed by the pressure gradient

(permeability controlled), concentration gradient (diffusivity controlled), and the time-dependent resistance of polymers to fluid flow, given by the mixture viscosity term.

$$\mathbf{v}^{\alpha,s} = -\varepsilon^\alpha \left(\frac{K^\alpha}{\mu^\alpha} \right) \nabla_E p^\alpha - \varepsilon^\alpha D^\alpha \nabla_E \varepsilon^\alpha - \frac{\varepsilon^\alpha K^\alpha}{\mu^\alpha} B^\alpha \nabla_E \varepsilon^\alpha, \quad \text{where } \alpha = w, o \quad (3)$$

The gas phase velocity is given by **Equation 4**,

$$\mathbf{v}^{g,s} = -\varepsilon^g \left(\frac{K^g}{\mu^g} \right) \nabla_E p^g \quad (4)$$

and the vapor phase velocity is given by **Equation 5**,

$$\mathbf{v}^{v,s} = \mathbf{v}^{g,s} + \mathbf{v}^{v,g} \quad (5)$$

where the second term on the RHS is due to binary diffusion of vapors with respect to gas (air+vapor mixture) and is expressed as **Equation 6** (25),

$$\mathbf{v}^{v,g} = -\frac{D^v}{\omega^v} \nabla_E \omega^v \quad (6)$$

where D^v is the vapor diffusivity. ω^v is the mass fraction of vapors in the air-vapor mixture and is given by, $\omega^v = \frac{\rho^v}{\rho^v + \rho^a}$, where ρ^v and ρ^a are the density of vapors and air, respectively.

2.4.2 Equations linking different variables and constitutive relations

Some of the variables which appear in the equations above are dependent on each other, and the equations relating those variables are discussed in this section. The total volume of an REV is occupied by the solid phase and pores. The porosity (ϕ) represents the total void space available for fluids to occupy (pores), and consequently, we can write **Equations 7** and **8** as:

$$\varepsilon^s + \phi = 1 \quad (7)$$

$$\varepsilon^w + \varepsilon^g + \varepsilon^o = \phi \quad (8)$$

Equation 7 can be used to replace ε^s and $\dot{\varepsilon}^s$ in **Equation 1** with $1 - \phi$ and $-\dot{\phi}$, respectively. Water vapors and air form a gas mixture in the pore volume, and this gives, $\varepsilon^g = \varepsilon^v = \varepsilon^a$. Dividing **Equation 8** by ϕ gives **Equation 9**,

$$S^w + S^g + S^o = 1 \quad (9)$$

where S^w , S^g and, S^o are the degrees of saturation for the liquid water, gas, and oil phases, respectively. Further, from Dalton's Law of partial pressures and the Ideal Gas Law we have **Equation 10** and **Equation 11**:

$$p^g = p^v + p^a \quad (10)$$

$$p^v = \frac{\rho^v RT}{M_w^v} \quad (11)$$

Here T is the temperature, M_w^v is the molecular weight of water vapors, and R is the universal gas constant.

The source/sink term, which determines the rate of evaporation at different spatial points, is given by **Equation 12** (17, 67, 142), where ζ (s^{-1}) is the evaporation rate constant, and ρ_{eq}^v is the equilibrium vapor density.

$${}^w \hat{e}^v = \zeta (\rho_{eq}^v - \rho^v) \quad (12)$$

Increasing ζ is expected to lead to faster evaporation, and for very high magnitudes of ζ , an equilibrium would exist between the water vapors and the liquid water. Zhang et al. (143) estimated the ζ value to

be of the order of 1 s^{-1} for evaporation of pure water. The value for ζ is expected to vary depending on the material and process (18, 142), but there is little information for it available in the literature. We inversely estimated the ζ value to be about 1.4 s^{-1} and performed a sensitivity test to show the significance of the ζ value. The results of the sensitivity test are presented and discussed in Section 4.3. It is interesting to note that, when implementing the transport partial differential equations (PDE), ζ appears in the source term. Large magnitudes of the source term often led to difficulties in convergence.

The difference between gas pressure and pressure in the liquid water and oil phases is given by water-air and oil-air capillary pressure, respectively. These relations are expressed as Equations 13 and 14, where p^{cw} and p^{co} are the water-air and oil-air capillary pressures, respectively. Further discussion on capillary pressure is provided in Section 2.8.1.

$$p^{cw} = p^g - p^w \quad (13)$$

$$p^{co} = p^g - p^o \quad (14)$$

The pore pressure is the effective pressure on the pore walls and is given by Equation 15 (52):

$$p_{pore} = S^w p^w + S^g p^g + S^o p^o \quad (15)$$

Next, by combining Equations 1 to 7, we obtain the equations for liquid water (Eq. 16), oil (Eq. 17), gas (Eq. 18), and water vapors (Eq. 19). Equations 16 to 19 are solved for ε^w , ε^o , p^g , and ρ^v , respectively.

$$\dot{\varepsilon}^w - \nabla_{\mathbf{E}} \cdot \left((\varepsilon^w)^2 \left(\frac{K^w}{\mu^w} \nabla_{\mathbf{E}} p^w + D^w \nabla_{\mathbf{E}} \varepsilon^w + \frac{K^w}{\mu^w} B^w \nabla_{\mathbf{E}} \dot{\varepsilon}^w \right) \right) + \frac{\varepsilon^w}{1 - \phi} \dot{\phi} = -\frac{1}{\rho^w} {}^w \hat{e}^g \quad (16)$$

$$\dot{\varepsilon}^o - \nabla_{\mathbf{E}} \cdot \left((\varepsilon^o)^2 \left(\frac{K^o}{\mu^o} \nabla_{\mathbf{E}} p^o + D^o \nabla_{\mathbf{E}} \varepsilon^o + \frac{K^o}{\mu^o} B^o \nabla_{\mathbf{E}} \dot{\varepsilon}^o \right) \right) + \frac{\varepsilon^o}{1 - \phi} \dot{\phi} = 0 \quad (17)$$

$$\dot{\varepsilon}^g \rho^g + \varepsilon^g \dot{\rho}^g - \nabla_{\mathbf{E}} \cdot \left((\varepsilon^g)^2 \rho^g \left(\frac{K^g}{\mu^g} \right) \nabla_{\mathbf{E}} p^g \right) + \frac{\varepsilon^g}{1 - \phi} \dot{\phi} \rho^g = {}^w \hat{e}^g \quad (18)$$

$$\dot{\varepsilon}^g \rho^v + \varepsilon^g \dot{\rho}^v - \nabla_{\mathbf{E}} \cdot \left(\rho^v \left((\varepsilon^g)^2 \left(\frac{K^g}{\mu^g} \right) \nabla_{\mathbf{E}} p^g + \left(\frac{\varepsilon^g D^v}{\omega^v} \right) \nabla_{\mathbf{E}} \omega^v \right) \right) + \frac{\varepsilon^g}{1 - \phi} \dot{\phi} \rho^v = {}^w \hat{e}^g \quad (19)$$

2.4.3 Energy balance equation

Three factors contribute to the efficiency of frying as a heating technique. First, the complete immersion of food in a bulk heating liquid acts as an energy reservoir, ensuring uniform heating. Second, the high heat capacity and density of oil make it a superior heating medium compared to hot air or steam (135). Third, the vigorous bubble generation during frying enhances the turbulence of the surrounding oil, which increases heat transfer rates. Additionally, the thermal expansion of oil creates buoyancy forces (105), promoting improved oil circulation as well as uniform mixing and recycling of hot oil. The combination of these factors result in frying having some of the highest heat transfer rates among common food processing operations, with the peak magnitude of the convective heat transfer coefficient during frying being on the order of $10^3 \text{ W/m}^2\text{K}$ (75).

Inside the food, heat is transported by both conductive and convective modes. Additionally, rapid evaporation of liquid water, particularly near the surface layers, occurs as these layers heat up the fastest. The two-scale convection-diffusion equation, which was solved for the temperature, T , is given by Equation 20 (23, 94, 120),

$$(\rho C_p)_{eq} \frac{\partial T}{\partial t} + (\rho C_p)_f \mathbf{v}^{f,s} \cdot \nabla_{\mathbf{E}} T = \nabla_{\mathbf{E}} \cdot (k_{eq} \nabla_{\mathbf{E}} T) - \lambda_v {}^w \hat{e}^g \quad (20)$$

where,

$$(\rho C_p)_{eq} = \sum_{\alpha=s,w,o,g} \varepsilon^\alpha \rho^\alpha C_p^\alpha$$

$$(\rho C_p)_f = \sum_{\alpha=w,o,g} \varepsilon^\alpha \rho^\alpha C_p^\alpha$$

$$k_{eq} = \sum_{\alpha=s,w,o,g} \varepsilon^\alpha k^\alpha$$

Here C_p is the specific heat, k is the thermal conductivity, and λ_v is the latent heat of vaporization. The two terms on the left hand side of Equation 20 represent energy storage and heat convection, respectively. The first term on the right hand side is the heat conduction term, whereas the second term is the phase change term. Since there are substantial temperature variations during frying, thermo-physical properties like thermal conductivity, specific heat, density and viscosity are expected to vary with temperature. The thermo-physical properties used in the current model are summarized in Table 1.

Table 1: Material properties.

Property		Expression or value	Reference
Thermal conductivity $\left(\frac{W}{mK}\right)$	Water	$-0.869 + 8.949 \times 10^{-3}T - 1.587 \times 10^{-5}T^2 + 7.975 \times 10^{-9}T^3$	132
	Vapors	$1.317 \times 10^{-4} + 5.150 \times 10^{-5}T + 3.896 \times 10^{-8}T^2 - 1.368 \times 10^{-11}T^3$	50
	Solid	0.21	67
	Oil	0.17	67
	Air	$-2.276 \times 10^{-3} + 1.155 \times 10^{-4}T - 7.902 \times 10^{-8}T^2 + 4.117 \times 10^{-11}T^3 - 7.439 \times 10^{-15}T^4$	132
	Gas	$\frac{X^v k^v}{X^v + X^a \phi^{va}} + \frac{X^a k^a}{X^v \phi^{av} + X^a}$ where $X^v = \frac{p^v}{p^g}, X^a = 1 - X^v$ $\phi^{av} = \frac{1}{\sqrt{8}} \left(1 + \frac{M_w^a}{M_w^v}\right)^{-0.5} \left(1 + \left(\frac{\mu_a}{\mu_v}\right)^{0.5} \left(\frac{M_w^v}{M_w^a}\right)^{0.25}\right)^2$ $\phi^{va} = \frac{1}{\sqrt{8}} \left(1 + \frac{M_w^v}{M_w^a}\right)^{-0.5} \left(1 + \left(\frac{\mu_v}{\mu_a}\right)^{0.5} \left(\frac{M_w^a}{M_w^v}\right)^{0.25}\right)^2$	25
Specific heat $\left(\frac{J}{kgK}\right)$	Water	$12010.147 - 80.407T + 0.3099T^2 - 5.3819 \times 10^{-4}T^3 + 3.6254 \times 10^{-7}T^4$	141
	Vapors	$13604.7344 - 90.4303506T + 0.27735566T^2 - 4.21264496 \times 10^{-4}T^3 + 3.18369497 \times 10^{-7}T^4 - 9.56147519 \times 10^{-11}T^5$	50
	Solid	1650	67
	Oil	2223	140
	Air	$1047.64 - 0.3726T + 9.4530 \times 10^{-4}T^2 - 6.0240 \times 10^{-7}T^3 + 1.2859 \times 10^{-10}T^4$	132
	Gas	$\omega^v c_p^v + \omega^a c_p^a$ where $\omega^v = \frac{\rho^v}{\rho^g}, \omega^a = 1 - \omega^v$	34

Density ($\frac{kg}{m^3}$)	Water	$273.15 K < T < 293.15 K: -950.704 + 18.923T - 6.037 \times 10^{-2}T^2 + 6.309 \times 10^{-5}T^3$ $T > 293.15 K: 432.257 + 4.969T - 1.340 \times 10^{-2}T^2 + 1.033 \times 10^{-5}T^3$	76
	Solid	1528	60
	Oil	$1106.1158 - 0.6414T$	55
	Air	$\frac{p^a}{R^a T}$	Ideal gas law
	Vapors at equilibrium	$\frac{p_{eq}^v}{R^v T}$	Ideal gas law
	Vapors in oil	$\frac{p_{ext}^v}{R^v T_{oil}}$	Ideal gas law
Dynamic viscosity ($Pa \cdot s$)	Water	$273.15 K < T < 413.15 K: 1.380 - 0.0212T + 1.3605 \times 10^{-4}T^2 - 4.6454 \times 10^{-7}T^3 + 8.9043 \times 10^{-10}T^4 - 9.0791 \times 10^{-13}T^5 + 3.8457 \times 10^{-16}T^6$ $413.15 K < T < 553.75 K: 4.0124 \times 10^{-3} - 2.1075 \times 10^{-5}T + 3.8577 \times 10^{-8}T^2 - 2.3973 \times 10^{-11}T^3$	132
	Vapors	$-1.4202 \times 10^{-6} + 3.8346 \times 10^{-8}T - 3.8522 \times 10^{-12}T^2 + 2.1020 \times 10^{-15}T^3$	50
	Oil	$0.1569 \times 10^{-5} e^{\left(\frac{3108}{T}\right)}$	108
	Air	$-8.3828 \times 10^{-7} + 8.3572 \times 10^{-8}T - 7.6943 \times 10^{-11}T^2 + 4.6437 \times 10^{-14}T^3 - 1.0659 \times 10^{-17}T^4$	132
	Gas	$\frac{X^v \mu^v}{X^v + X^a \phi^{v_a}} + \frac{X^a \mu^a}{X^v \phi^{a_v} + X^a}$	25
Molecular weight ($\frac{kg}{mol}$)	Vapors	0.018	100
	Dry air	0.02897	100
Gas constants	Ideal gas constant	$R = 8.31446 \frac{J}{molK}$	100
	Gas constant for air	$R^a = \frac{R}{M_w^a}$	
	Gas constant for vapors	$R^v = \frac{R}{M_w^v}$	
Diffusivity ($\frac{m^2}{s}$)	Water	$0.9 \times 10^{-10} e^{-2.8+2.0M^w}$	Based on Ni (92)
	Vapors	$(-2.775 \times 10^{-6} + 4.479 \times 10^{-8}T + 1.656 \times 10^{-10}T^2) \epsilon^{g \frac{4}{3}}$	91, 92, 142
Permeability (m^2)	Gas	$K^g = K_i^g K_r^g$ where $K_i^g = 3 \times 10^{-14} \frac{\phi^3}{(1-\phi)^2} m^2, K_r^g = 1 - 1.1S^w$	61, 67, 93
	Water	$K^w = \frac{D^w \mu^w}{E}$	4, 120
	Oil	$K^o = 10^{-17} m^2$	67
Viscoelastic Parameters	Viscosity of dashpot in Maxwell element	$\eta = 1.72 \times 10^8 Pa \cdot s$	107
	Viscoelastic parameter (J_0) for spring in Maxwell element	$M^w \leq 0.4: J_0 = J_{0,cf}(0.1297 + 1.6967M^w)10^{-3} Pa^{-1}$ $M^w > 0.4: J_0 = J_{0,cf}(0.8823 - 0.1849M^w)10^{-3} Pa^{-1}$	Equation fitted to the data of Sandhu & Takhar (107)

	$J_{0,cf}$	0.33	Estimated inversely
	$J_{0,avg}$	$4.0969 \times 10^{-4} Pa^{-1}$	107
	Young's modulus (E)	$\frac{1}{J_0}$	118
	Bulk modulus of the spring in the Maxwell element	$K_v = \frac{E}{3(1-2\nu)}$	118
Latent heat of vaporization		$\lambda_v = 2.26 \times 10^6 \frac{J}{kg}$	97
Evaporation rate constant		$\zeta = 1.4 s^{-1}$	Estimated inversely
Mixture viscosity		$B^\alpha = 0.8 \times 10^{-6} \times \frac{E}{E} Pa.s$	120
Poisson ratio		$\nu = 0.492$	51

2.5. Equations for volume changes during frying

Phenomena such as water loss, gas expansion, and rise in capillary pressure lead to the development of mechanical stresses within the porous food material. The pore pressure is used as the variable governing the deformation of the porous food matrix. The stress due to pore pressure (σ_{pore}) represents the stress exerted on the pore walls by the fluids occupying the pores, as given by Gray and Schrefler (64) (Eq. 21):

$$\sigma_{pore} = -p_{pore}I \tag{21}$$

Many fruits and vegetables, including potatoes, have been shown to exhibit viscoelastic behavior (11). Viscoelastic materials show both viscous (fluid-like) and elastic (solid-like) properties when undergoing deformation. Such materials respond to applied stress in a time-dependent manner. Here, we use Maxwell's model (Fig. 2) to study the viscoelastic response of food during frying. Maxwell's model is an in-series combination of a spring and a dashpot. The stress acting across the spring and the dashpot is the same and is equal to the stress applied across the combination. The total volumetric strain ($\epsilon_{vol,total}$) across the combination is given by Equation 22, where $\epsilon_{vol,1}$ is the strain across the spring and $\epsilon_{vol,2}$ is the strain across the dashpot.

$$\epsilon_{vol,total} = \epsilon_{vol,1} + \epsilon_{vol,2} \tag{22}$$

The strains across the spring and dashpot can be calculated as follows:

$$\epsilon_{vol,1} = \frac{\sigma_{vol}}{K_v} \tag{23}$$

$$\dot{\epsilon}_{vol,2} = \frac{\sigma_{vol}}{\eta} \tag{24}$$

where, σ_{vol} is the volumetric stress, K_v is the bulk modulus of the spring, and η is the viscosity of the dashpot. σ_{vol} is calculated using the pore pressure, which acts normally in all directions:

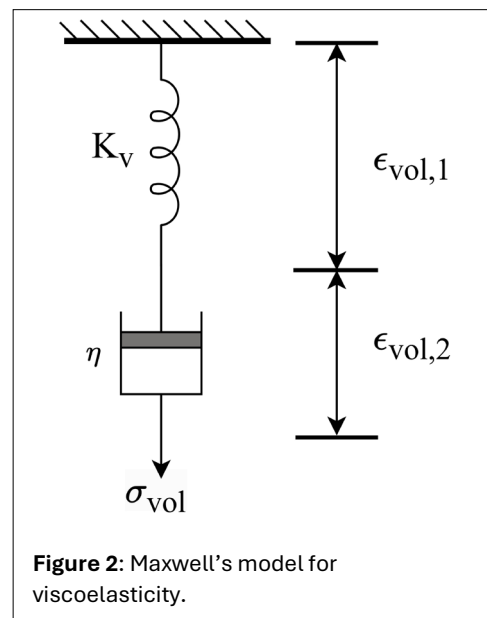


Figure 2: Maxwell's model for viscoelasticity.

$$\sigma_{vol} = \frac{\sigma_{11} + \sigma_{22} + \sigma_{33}}{3} - p_{pore} \mathbf{I} \quad (25)$$

The bulk modulus of the spring and viscosity of the dashpot were calculated based on the viscoelastic model parameters estimated by Sandhu and Takhar (107) as a function of moisture content for fried potato discs ([Table 1](#)).

2.6. Conversion from Eulerian to Lagrangian coordinates

The pore pressure-driven spatial and temporal changes in the structure of the porous matrix make frying a moving boundary problem. Solving the equations using an Eulerian framework would require a continuously deforming mesh, which would increase the computation times (119). An alternative approach is to transform the equations to Lagrangian coordinates and obtain the solution using a stationary reference material configuration (119). The initial state of the system (at $t = 0$ s) is chosen as the reference frame. The details about the conversion from Eulerian to Lagrangian coordinates are presented in the [Appendix](#) (available online [here](#)).

$$\nabla_E = \frac{1}{\xi} (\nabla_L) = \left(\frac{1 - \phi}{1 - \phi_0} \right)^{\frac{1}{3}} \nabla_L \quad (26)$$

The gradient operator in Eulerian coordinates, ∇_E , can be converted to the gradient operator in Lagrangian coordinates (∇_L) using [Equation 26](#), and is used to replace ∇_E in [Equations 16](#) to [Equation 19](#) with ∇_L .

2.7. Initial and boundary conditions

The initial volume fraction of oil, ε_i^o , in the porous matrix was taken to be 0 as raw potatoes have negligible oil content. The initial volume fraction of gas in raw potato, ε_i^g , is about 0.05 (113, 148). The initial mass fraction of liquid water on a dry basis can be represented as [Equation 27](#):

$$M_i^w = \frac{\rho_i^w \varepsilon_i^w}{\rho^s \varepsilon_i^s} \quad (27)$$

Rearranging, we obtain [Equation 28](#):

$$\varepsilon_i^w = \frac{M_i^w \rho^s \varepsilon_i^s}{\rho_i^w} = \frac{M_i^w \rho^s (1 - \varepsilon_i^w - \varepsilon_i^g - \varepsilon_i^o)}{\rho_i^w} \quad (28)$$

Further simplifying [Equation 28](#) to find an explicit expression for ε_i^w , we obtain [Equation 29](#):

$$\varepsilon_i^w = \frac{M_i^w \rho^s (1 - \varepsilon_i^g - \varepsilon_i^o)}{\rho_i^w + M_i^w \rho^s} \quad (29)$$

For $M_i^w = 4.20$ g water/g solids (110), using [Equation 29](#), we get $\varepsilon_i^w = 0.822$. The initial porosity can be determined using, $\phi_i = \varepsilon_i^w + \varepsilon_i^g + \varepsilon_i^o$. The frying is carried out under atmospheric pressure, and the initial gas pressure in the matrix is $p_i^g = P_{atm}$. The initial temperature inside the matrix is $T_i = 291.5$ K (110), and the initial vapor density is estimated as $\rho_i^v = \frac{p_{eq,i}^v}{R^v T_i}$.

The following boundary conditions were used:

$$\varepsilon_{surface}^w = \varepsilon_{oil}^w \text{ for } \text{Equation 16} \quad (30)$$

$$q^o = h_m^o (S^o - S_{oil}^o) \text{ for } \text{Equation 17} \quad (31)$$

$$p_{surface}^g = P_{atm} \text{ for } \text{Equation 18} \quad (32)$$

$$q^v = h_m^v(\rho^v - \rho_{oil}^v) \text{ for Equation 19} \tag{33}$$

$$q^T = h_T(T - T_{oil}) + e\sigma(T^4 - T_{oil}^4) \text{ for Equation 20} \tag{34}$$

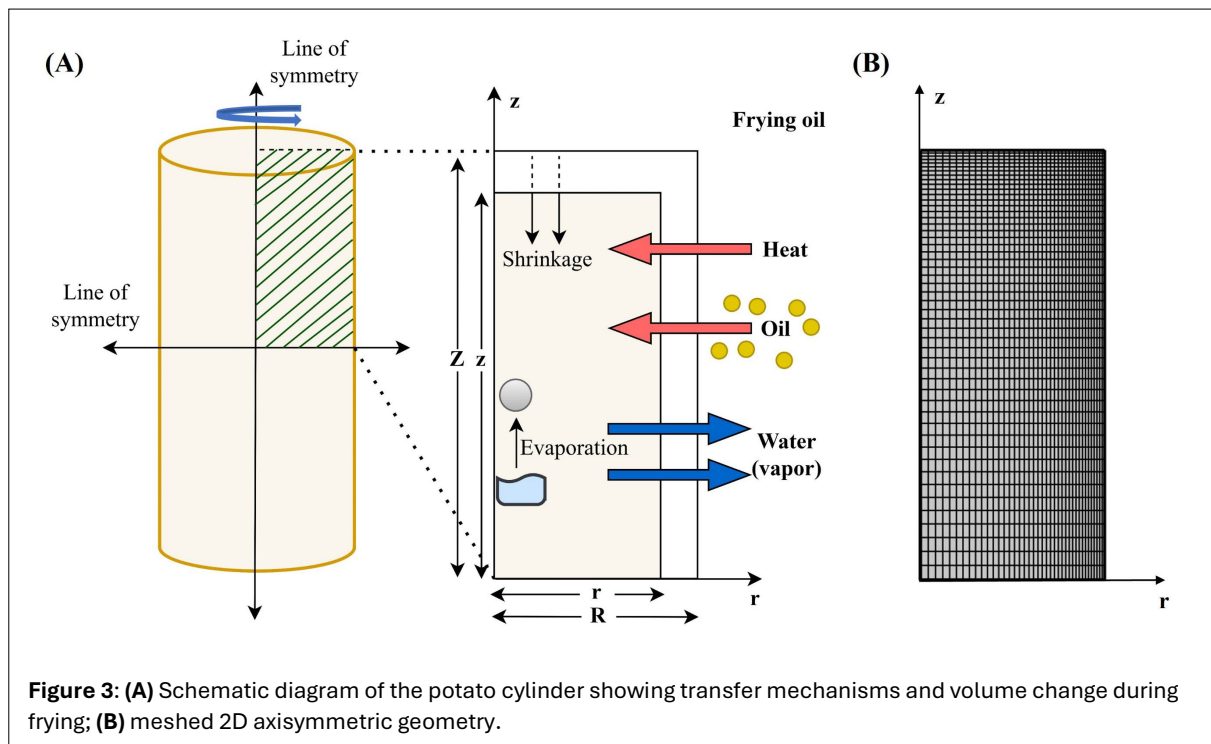


Figure 3: (A) Schematic diagram of the potato cylinder showing transfer mechanisms and volume change during frying; (B) meshed 2D axisymmetric geometry.

The value of the constants, and heat and mass transfer coefficients that appear in **Equations 30 to 34** are summarized in **Table 2**. The volume fraction of water on the surface of the sample is assumed to be equal to the volume fraction of water in the bulk oil (**Eq. 30**). The mass flux of oil is driven by the oil saturation gradient (**Eq. 31**). The frying is carried out at atmospheric pressure, thus the gas pressure at the surface is equal to 1 atm (**Eq. 32**). The mass flux of vapors is driven by the vapor density gradient (**Eq. 33**). Heat transfer at the surface is driven by convection and radiation, represented by the first and second terms on the right hand side of **Equation 34**, respectively. The no-flux boundary conditions are used for the boundaries lying on the lines of symmetry (**Fig. 3A**).

Table 2: Supporting expressions required for solving the model.

Property	Expression or value	Reference
Saturated vapor pressure	$p_{sat} = \exp\left(-\frac{6096.9385}{T} + 21.2409642 - 2.711193 \times 10^{-2}T + 1.673952 \times 10^{-5}T^2 + 2.433502\log(T)\right) Pa$	100
Water activity	$a_w = \frac{-2M^w + M^w C_1 - C_1 M_{10} + \sqrt{4M^w C_1 M_{10} + M^{w2} C_1^2 - 2M^w C_1^2 M_{10} + C_1^2 M_{10}^2}}{2M^w(-1 + C_1)K_1}$ <p>where $C_1 = 0.867 \times 10^{-3} e^{\frac{2999}{T}}$, $K_1 = 0.825$, $M_{10} = 0.0575$</p>	136
Vapor pressure at equilibrium	$p_{eq}^v = p_{sat} a_w$	34
Water phase capillary pressure	$p^{cw} = 101325 [AS_e^w \exp(-BS_e^w) + C(1 - S_e^w)S_e^{w-D}] (1 - 2.79 \times 10^{-3}(T - 273)) Pa$ <p>where $S_e^w = \frac{S^w}{S_s^w}$, $S_s^w = 0.94$, $A = 27.12$, $B = 5.939$, $C = 0.782$, $D = 1.4$ (estimated inversely)</p>	26, 78

Oil phase capillary pressure	$p^{co} = \frac{2\gamma \cos \theta}{R_{pore}}$ where $\gamma = 0.024 \frac{N}{m}$, $R_{pore} = 12 \times 10^{-6} m$, $\theta = 38^\circ$	31, 101
Atmospheric pressure	$P_{atm} = 101325 Pa$	100
Vapor pressure in oil	$p_{ext}^v = 0.00001 Pa$	Negligible value assumed
Mass transfer coefficient for vapors	$h_m^v = 0.2 - \frac{(0.2-0.0013)t}{960} \frac{m}{s}$	Adapted from Halder et al. (67)
Mass transfer coefficient for oil	$h_m^o = \frac{Sh \times D^{o,o}}{L} \frac{m}{s}$ where $Sh = 0.82 R_e^{\frac{1}{2}} S_c^{\frac{1}{3}}$, $R_e = \frac{\rho^o V L}{\mu^o}$, $S_c = \frac{\mu^o}{\rho^o D^{o,o}}$, $V = 5 \times 10^{-2} \frac{m}{s}$, $D^{o,o} = 3.5 \times 10^{-10} \frac{m^2}{s}$	38, 100
Liquid water volume fraction in bulk oil	$\varepsilon_{oil}^w = 0.01$	120
Oil saturation in bulk oil	$S_{oil}^o = 0.99$	Estimated using ε_{oil}^w value
Heat transfer coefficient	$h_T = 144 - 904 W/m^2 K$ Data of Farinu and Baik (2007) were used	58
Temperature of the oil	T_{oil} at the start of frying was 193°C. Measured temperature profile of the bulk oil was used in the model.	Measured
Emissivity	$e = 0.9$	84
Stefan-Boltzmann Constant	$\sigma = 5.670373 \times 10^{-8} \frac{W}{m^2 K^4}$	100

Material properties

The material properties used in the model are summarized in **Table 1** and **Table 2**. In the next section, we provide a discussion of some of these properties.

2.8.1 Capillary pressure

Capillary pressure is well understood and extensively researched in fields dealing with unsaturated fluid flow, such as wood, soil, and geological sciences. However, despite its relevance to unsaturated transport and capillary pressure-driven liquid movement in many porous foods, there is a lack of capillary pressure data specifically for food systems. The soft nature of food limits the application of methods that use high applied pressures or centrifugal forces to drive liquid flow from the porous matrix (111). Furthermore, foods may undergo microbial contamination or swelling during the equilibration time (128). In the absence of appropriate capillary pressure data, mathematical models for foods have relied on simplifications, such as assuming a combined diffusion-like transport for both liquid water and gas phases (33, 112), or employing a capillary diffusion approach (65, 67). Regardless of which simplification is used, it is still necessary to estimate a diffusivity value, ideally as a function of moisture content and temperature. Shah and Takhar (111) reviewed the commonly used mathematical models for unsaturated food systems and discussed their assumptions and limitations.

In the absence of capillary pressure data for food systems, we adopted the following equation (Eq. 35) as developed by Bonneau and Puiggali (26) for pinewood:

$$p^{cw} = 101325[AS_e^w \exp(-BS_e^w) + C(1 - S_e^w)S_e^{w-D}](1 - 2.79 \times 10^{-3}(T - 273)) \text{ Pa} \quad (35)$$

Here, the water phase capillary pressure (p^{cw}) is given as a function of the saturation of water and temperature (78). The values of the fitting parameters (A , B , C , and D) are summarized in Table 2.

2.8.2 Permeability and Diffusivity

According to Darcy's Law (Eq. 3), permeability controls the pressure gradient-driven transport in porous media. As a result, permeability values are essential to our model solution. The complex structure of food and the dynamic nature of the changes that occur during processing makes the estimation of permeability difficult. Datta (43) estimated the permeability for saturated samples of raw potato slices using a pressure-based method. The flow rate of water moving through a sample under pressure is measured, and the permeability is estimated using the Darcy's law. Datta (43) found that the permeability of potatoes varies between 10^{-17} to 10^{-19} m^2 . An increase in permeability with applied pressure was observed for some samples. Additionally, swelling was observed in the potato samples during the experiments, which could affect the estimated permeability values. These factors can explain the variability in permeability data reported in this study (43) and other permeability estimation studies for foods.

Dadmohammadi et al. (40) estimated the permeability of saturated raw potato discs using the pressure-based direct estimation method, an indirect nuclear magnetic resonance (NMR)-based method, and a phenomenological approach based on approximating the porous media as a bundle of tubes. The latter method is also referred to as the Carman-Kozeny approach. The permeability of raw potato samples was found to be of the order of 10^{-18} m^2 using the three methods.

A range of temperature-dependent changes accompanies the heating of potato samples, including gas and liquid expansion, cell swelling, cell rounding, cell separation, starch gelatinization, and, eventually, cell rupture (40). Some of these changes increase permeability, whereas others decrease it. The overall change in permeability is thus a cumulative result of these phenomena. The gas (air, water vapor, or CO_2 from respiration) and liquid (water) present in the extracellular spaces expand upon heating, which is expected to increase the volume of the pore space, thereby increasing the permeability for extracellular fluid flow.

The pectin-mediated cell adhesion (41) undergoes changes at higher temperatures, and eventually, there is cell separation. Cell separation provides more pathways for fluid movement, and as a result, the permeability increases further. At elevated temperatures between 50 to 100°C , Dadmohammadi et al. (40) estimated the water permeability to be approximately 10^{-15} m^2 . Using the pressure-based direct estimation method, Alam et al. (9) found the water permeability values for potato discs to be between $2 \times 10^{-15} \text{ m}^2$ to $4 \times 10^{-15} \text{ m}^2$ for samples heated to temperatures between 70 to 80°C . In Alam et al. (9), pressures up to 345 kPa were applied to drive fluid flow.

On the other hand, the swelling of cells and increased turgor pressure due to water uptake can restrict the extracellular movement of fluids, which is expected to decrease permeability. When cooking times are longer, cell rupture may occur. The cell contents, including the starch granules, are released into the extracellular spaces. As a result, the available pore volume and pathways for fluid flow may decrease, and thus cause a decrease in permeability.

In this study, Equation 36, which appears in the HMT-based derivation of transport equations (4, 120), was used to calculate the water permeability:

$$K^w = \frac{D^w \mu^w}{E} \quad (36)$$

The liquid water diffusivity (D^w) expression based on Ni (92) was used and is listed in Table 1. Based on the above equation, the K^w value used in this study varied spatially and temporally, and ranged from

approximately 10^{-15} m^2 to 10^{-19} m^2 . This is within the range of the experimentally estimated water permeability values for potatoes (9, 40, 43). Sensitivity testing was performed for K^w and the results are discussed in Section 4.3.

Very little information is available on oil permeability (K^o) in porous foods. A K^o value of 10^{-17} m^2 (67) was used in the model, and sensitivity tests were performed to show the effect of the K^o value on the estimated oil content. Studying oil transport during frying has proven to be complicated. Oil penetration into the porous matrix is significantly affected by the food's microstructure and how it evolves with frying time.

Bouchon et al. (28) showed that only a minor fraction of oil penetrates potato samples during the immersion phase of frying, whereas significant oil uptake occurs during the cooling phase. Three oil fractions were identified: structural oil (absorbed during the immersion phase), penetrated surface oil (penetrated during the cooling phase), and surface oil. The surface oil was determined by washing the fried potato samples in petroleum ether for 1 s. The total oil content of the fried potato samples (excluding the surface oil) was determined by the Soxhlet method. Oil dyed with Sudan Red B was added towards the end of frying as an indicator, and the dye concentration in the extracted oil was determined by measuring the absorbance at 509.6 nm. The dye-stained oil represented the penetrated surface oil; the remaining portion of the extracted oil was the structural oil. It was found that the structural oil accounted for less than 5% of the final oil content in the fried samples (28). On the other hand, the penetrated surface oil content increased with frying time and accounted for up to 89% of the total oil absorbed by the samples. It was concluded that surface damage and porosity increase with frying time, allowing more oil to penetrate during the cooling phase (28). Therefore, while only a minor fraction of oil enters deeper in the food during the immersion phase, the frying-driven changes in the food microstructure have a significant impact on the oil content of the final product. Additionally, pressure and temperature changes during frying play a critical role in governing the oil uptake (135).

These observations motivated numerous studies focused on elucidating the oil uptake mechanisms, including those of He et al. (73), Patsioura et al. (98, 99), Touffet et al. (126), Vauvre et al. (133, 134), and Ziaifar et al. (147). While there may not be a complete consensus on the relative importance of all mechanisms, pressure-governed oil transport is considered to be the most important mechanism. Vaporization, gas expansion, and restriction to the growth of water bubbles by the solid matrix (146) lead to high pressures in the porous matrix during frying. The high pressures are expected to prevent oil penetration.

Using an oil dyeing technique, Touffet et al. (126) found that thawing of parfried-frozen potato samples reduced oil absorption during the immersion stage of frying. It was suggested that the presence of ice in frozen samples impacted the pressure development. Compared to fresh or thawed samples, the pressure rise in frozen samples is delayed, allowing the oil to enter the food (99). This highlighted the significance of pressure-governed oil transport.

However, there is a lack of evidence supporting the diffusive transport of oil during frying. It is common to find Fick's Law of diffusion used to model oil transport in the frying literature (15, 35, 42). Such models define an effective oil diffusivity, which is determined experimentally. The caveat here is that distinct mechanisms of oil uptake are lumped together as effective diffusion. Fick's Law-based modeling of lumped diffusive transport is only analogous to concentration gradient-driven diffusion.

Diffusive transport of oil, in the absence of pressure-driven transport, would make the oil uptake continuous (99). This, however, is contrary to the discontinuous oil uptake behavior observed experimentally (73). Additionally, the penetration depth of oil estimated based on diffusive transport ranged from a few millimeters up to centimeters (98). This conclusion is not entirely accurate, as experimental studies have shown that oil penetration in potatoes is restricted to just a few layers beneath the surface (28, 29).

Insights into oil transport in porous materials can also be drawn from petroleum and soil sciences. Oil spills during crude oil exploration, transportation, and processing contaminate the environment and

groundwater (79, 82). This poses safety concerns and has led to numerous studies on the movement of spilled crude oil in soils (3, 72, 102). Oghenejoboh and Puyate (95) conducted experiments to analyze the movement of six crude oil samples with different physical properties spilled in top (loamy-sand) soil. During a 25-day period, the oil did not travel beyond a few centimeters from the point of spillage in the horizontal (longitudinal) direction. In contrast, the oil movement in the vertical direction was significantly pronounced for all samples. Oghenejoboh and Puyate (95) concluded that the horizontal movement of crude oil, governed by concentration gradient-driven diffusion, was negligible compared to vertical movement, which, in addition to concentration gradient, is driven by gravitational forces.

Similar studies for analyzing oil movement in porous food materials are encouraged to resolve the significance of diffusive transport, although its magnitude is expected to be low. Given the current lack of evidence supporting diffusive transport compared to pressure-driven flow of oil during frying, we exclude the diffusion term from the Darcy's law (Eq. 3) for oil. By doing so, we also highlight the agility and adaptability of mechanistic models. The importance of experimental studies in complementing and guiding model development is further emphasized.

Gas flow plays a critical role in unsaturated transport processes because the gas pressure gradient drives the movement of the liquid phases (water and oil phases in the case of frying). Additionally, evaporation and subsequent movement of vapor affect heat transfer within the porous matrix. Two properties required for modeling gas (air and vapors) transport are gas permeability (K^g) and vapor diffusivity (D^v). The following expressions (Eq. 37, 38, and 39) were used for calculating gas permeability (61, 67, 93):

$$K^g = K_i^g K_r^g \quad (37)$$

$$K_i^g = 3 \times 10^{-14} \frac{\phi^3}{(1 - \phi)^2} \text{ m}^2 \quad (38)$$

$$K_r^g = 1 - 1.1S^w \quad (39)$$

where K_i^g is the intrinsic gas permeability and K_r^g is the relative gas permeability. The minimum value of K_r^g was restricted to a non-negative, non-zero value of 0.05, estimated inversely. The vapor diffusivity (D^v) expression of Nellis and Klein (91) was used in the model and is provided in Table 1.

3. MATERIALS AND METHODS

3.1. Experimental procedures

Potato cylinders, 44 mm in length and 18 mm in diameter, were cut from fresh whole potatoes using a stainless-steel fruit corer. The cut samples were then blanched in boiling water for 2 minutes before frying. The samples were fried in a commercial blend of frying oil at a temperature of 193°C for a maximum duration of 300 s. The fried samples were immersed in liquid nitrogen for 10 s to arrest the cooking. The moisture and oil content of the samples were determined using the convection oven method and the Soxhlet method, respectively. The sample weights were recorded using an electronic balance¹ with a maximum error of $\pm 1.0 \text{ mg}$. Real-time temperature and pressure measurements were made at the center of the sample. The temperature measurements were made using three K-type thermocouples² with an accuracy of about $\pm 1.1 \text{ }^\circ\text{C}$ inserted in three samples. The pressure measurements were made using a fiber optic pressure sensor³ with an error of $\pm 5 \text{ kPa}$. The sensors were connected to data loggers, and the extracted data was stored in Microsoft Excel for further analysis.

Fried samples continued to undergo volume changes after removing them from the frying oil. It is thus vital that volume measurements of the sample are made quickly. To ensure rapid volume measurement,

¹ U.S. Solid, Cleveland, Ohio, U.S.A. (model no. USS-DBS8)

² PerfectPrime, New York, New York, U.S.A.

³ FOP-MH-NS-556A: FISO Technologies Inc., Quebec, Canada

a liquid displacement technique was used with n-Heptane ($\rho = 679.5 \text{ kg/m}^3$ at 25°C) as the solvent. Additional details about the experimental procedures can be found in Shah and Takhar (110).

3.2. Numerical solution

The finite element method (FEM) was used to solve the mathematical model. The FEM approach is a numerical technique that is capable of solving a wide range of PDEs (77). It can be employed for complex geometries and can be utilized for coupling equations for various physics modes such as heat transfer, porous media, structural mechanics, etc. A commercial FEM package⁴ was used to set up the model, solve the equations, and post-process the results. Instead of solving for the entire 3D cylindrical geometry, the model was solved for an axisymmetric rectangular geometry (2D) (Figure 3A). By assuming symmetry about the horizontal line passing through the center of the cylinder, the model was solved only for the upper half of the original geometry. This approach significantly reduced the computational load, making it feasible to conduct additional simulations.

A crucial step in the FEM approach is the discretization of the computational domain. A mapped mesh (Figure 3B) with 2000 quadrilateral elements, 180 edge elements, and 4 vertex elements was used. A non-uniform element distribution (element ratio of 3 and 5 in r and z directions, respectively) was used to have more elements near the surface exposed to oil. Rapid changes are expected in the surface layers, and a higher element density is needed to resolve such changes optimally. A mesh independence study was performed to ensure that the model results do not vary significantly with the number of elements. The number of elements in r and z directions were changed by $\pm 10\%$. Decreasing the number of elements by 10% in both directions resulted in a coarser mesh with 1620 quadrilateral elements, i.e., a 19% decrease in the total number of elements. Increasing the number of elements by 10% in both directions resulted in a finer mesh with 2420 quadrilateral elements, i.e., a 21% increase in the total number of elements. Simulations conducted using the coarser and finer mesh led to an average change in the value of dependent variables by 1.83% and 1.30%, respectively. Therefore, the mesh with 2000 quadrilateral elements was considered optimum for conducting simulations.

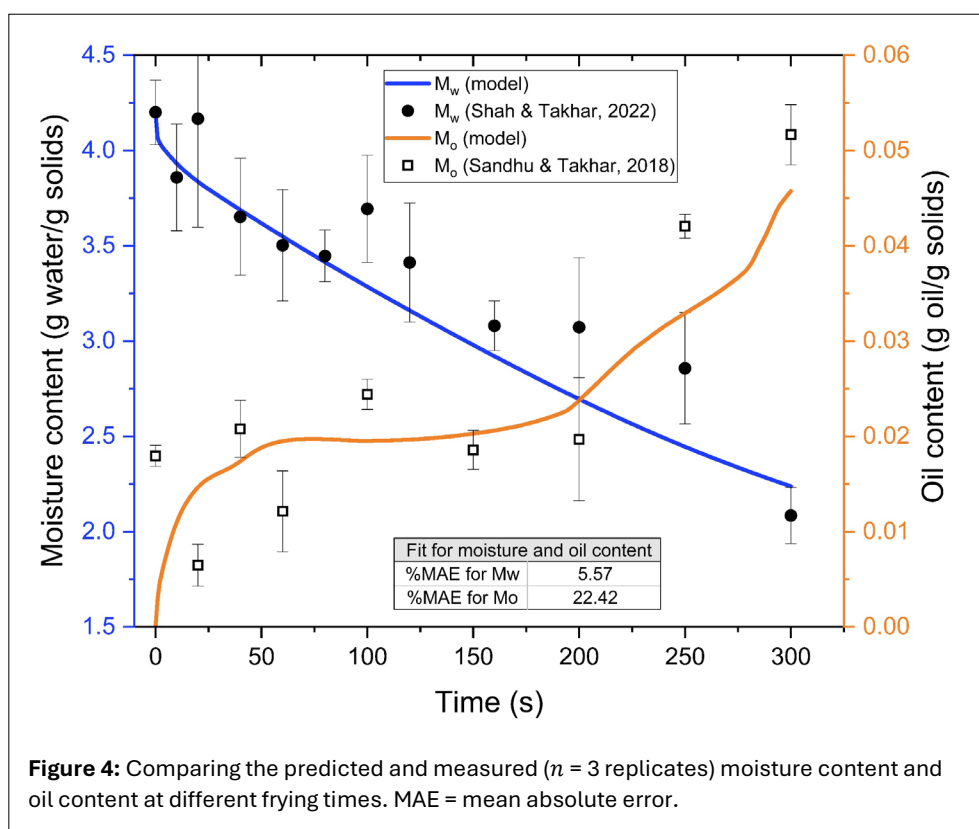


Figure 4: Comparing the predicted and measured ($n = 3$ replicates) moisture content and oil content at different frying times. MAE = mean absolute error.

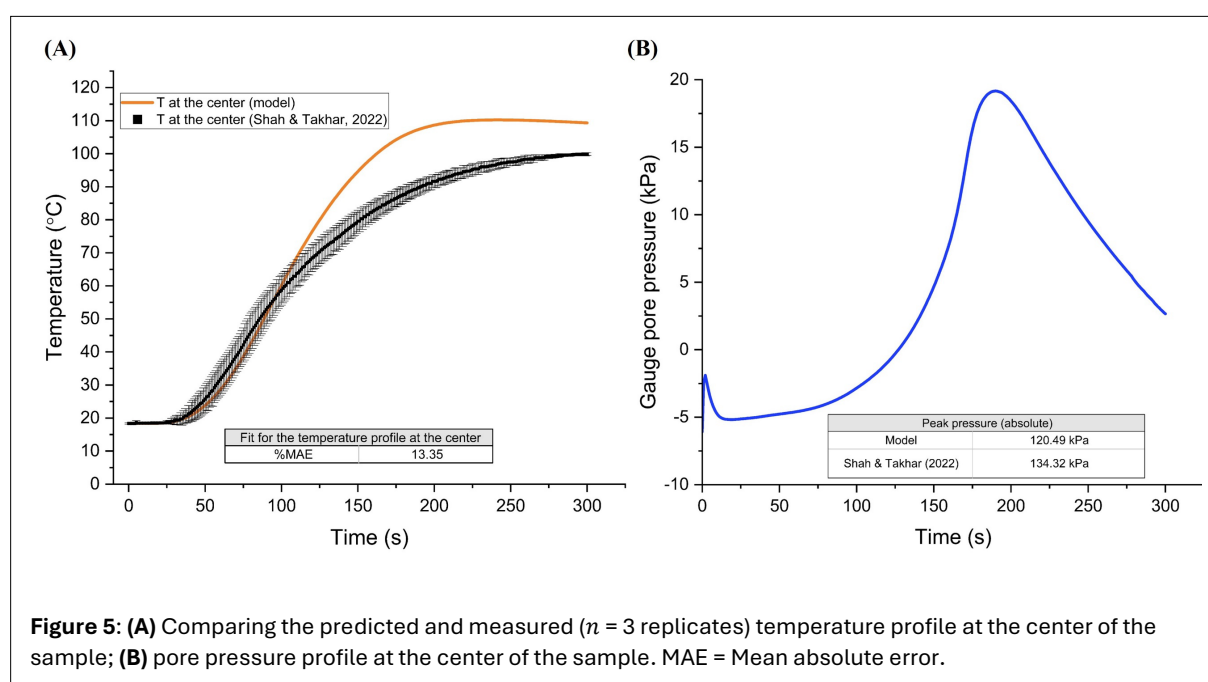
⁴ COMSOL Multiphysics® v. 6.1: COMSOL, Inc., Burlington, MA, USA

The backward differentiation formula (BDF) method, which is an implicit method for numerical integration, was used for time-stepping. The maximum and minimum order for the BDF method was set to 2 and 1, respectively. The solver was enabled to select the appropriate step size automatically. MULTifrontal Massively Parallel Solver (MUMPS) (12), which is a direct solver based on Gaussian elimination, was used for solving the sparse linear equations, which are characteristic of utilizing the finite element method (77). The automatic Newton method was selected as the nonlinear method in the software. The solver was allowed to automatically determine a damping factor for each iteration of Newton's method. It took 12 to 18 mins for each run to simulate 300 s of frying time on a workstation with an AMD Ryzen 7 processor with a clock speed of 3.60 GHz and 32 GB RAM.

4. RESULTS AND DISCUSSION

4.1. Results

The model predictions were validated using the experimental results available in the frying literature, particularly those of Shah and Takhar (110). The percent mean absolute error (%MAE) was calculated, and a good agreement was found between the model predictions and experimental results (Fig. 4, Fig. 5, Fig. 6). The %MAE for moisture content, oil content, and temperature is 5.57%, 22.42%, and 13.35%, respectively. The model performance is expected to improve with the availability of more data for material properties like permeability and capillary pressure. The potential reasons for some of the model inaccuracies and recommendations for improving model performance are discussed in more detail in Section 4.4.



The sample temperature, pressure, and volume continued to change after the sample was removed from the fryer (110). The fried potato cylinders continued to shrink after removal from the fryer as the pressure in the porous matrix dropped due to water vapor collapse. Shah and Takhar (110) measured volume change using a modified liquid displacement method which allowed for rapid volume measurements. However, even with the rapid method, it is not feasible to instantaneously capture the sample volume after frying. As a result, differences between measured and model-computed volume changes are expected (Fig. 6).

Spatial profiles were created for model variables like moisture content, oil content, pressure, and evaporation rate (Fig. 7, Fig. 8, Fig. 9, Fig. 10). The spatial profiles were plotted as a function of the Lagrangian coordinates. To generate such profiles experimentally would take extensive testing, which

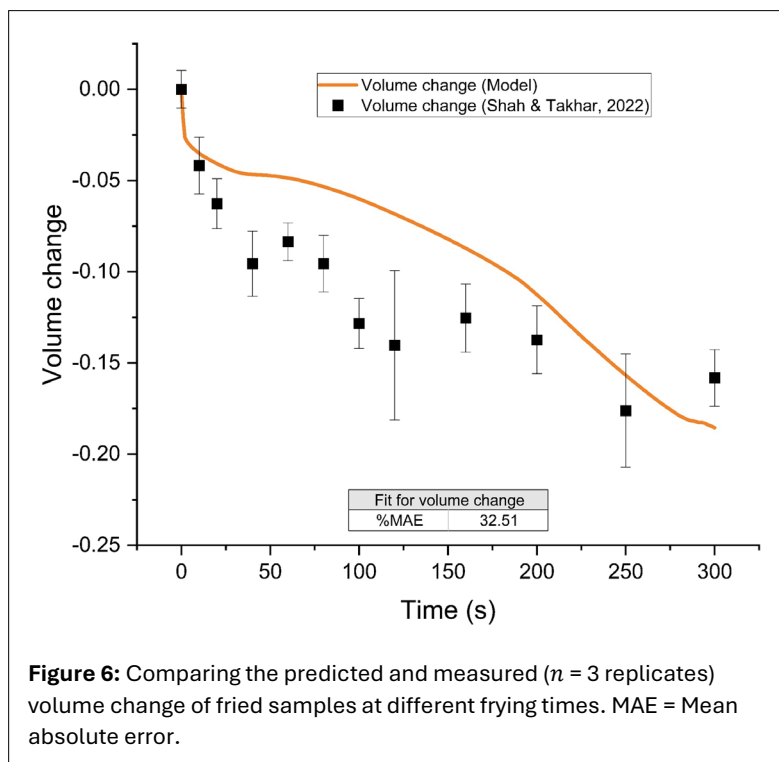


Figure 6: Comparing the predicted and measured ($n = 3$ replicates) volume change of fried samples at different frying times. MAE = Mean absolute error.

may be expensive and is not always feasible. The spatial profiles provide an intuitive understanding of the different phenomena occurring during frying. These profiles are discussed in detail in the next section.

4.2. Discussion

During frying, phenomena such as water loss, oil penetration, temperature rise, pressure changes, and volume changes occur simultaneously, with intricate coupling occurring between the different variables. This complexity makes modeling challenging, but the insights generated from this exercise are valuable. To highlight the coupled nature of these phenomena, we describe the frying

process as a series of changes beginning with the rapid heat transfer from the hot oil.

There is a steep drop in moisture content during the early stages of frying (Fig. 4, $t < 25$ s). The rapid heat transfer to the moisture-rich potato samples causes a rapid vaporization of the surface water, which is lost to the bulk oil. Some authors refer to this stage as superficial or surface boiling (59, 135). The bubbles initially seen around the food are that of the vaporized surface water.

The initial moisture loss from the food is controlled by the external heat transfer. While the steam bubbles lead to more oil movement, their crowding around the food adds to the heat transfer resistance (105). The bubble velocity, frequency, flow direction, and oil agitation are important factors affecting the heat transfer rate (58).

There is rapid oil uptake during the initial frying stages (Fig. 4, $t < 50$ s). Injuries to the cellular structure near the surface are unavoidable during sample extraction from whole potatoes. This, combined with pores left empty by the escaping water from the surface, allows the entry of oil. During the initial phases,

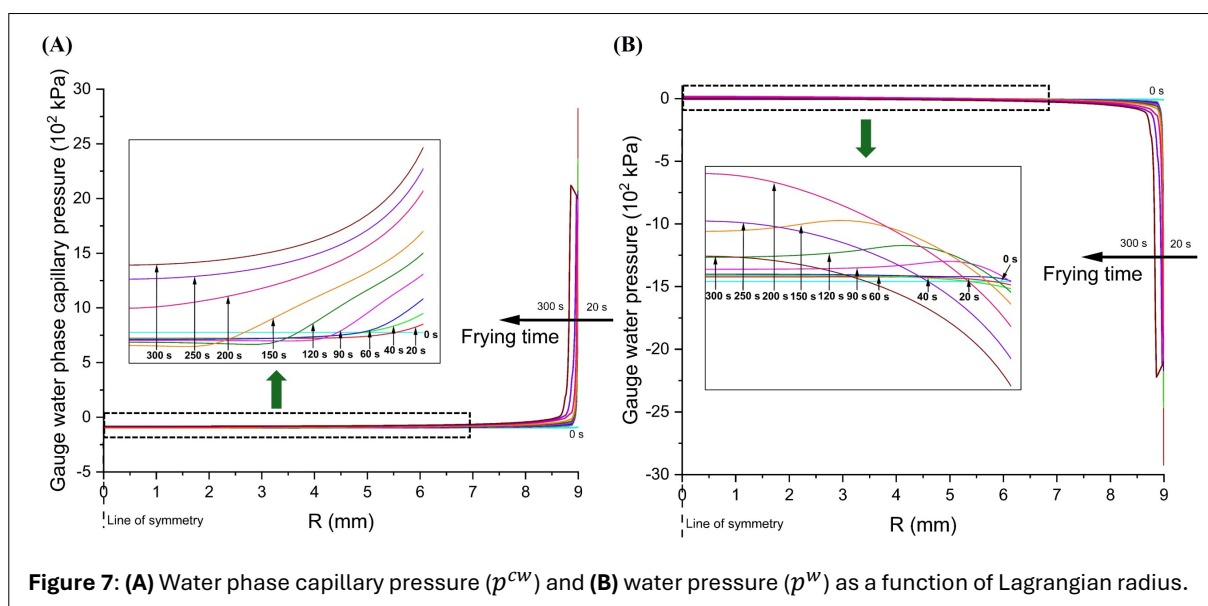
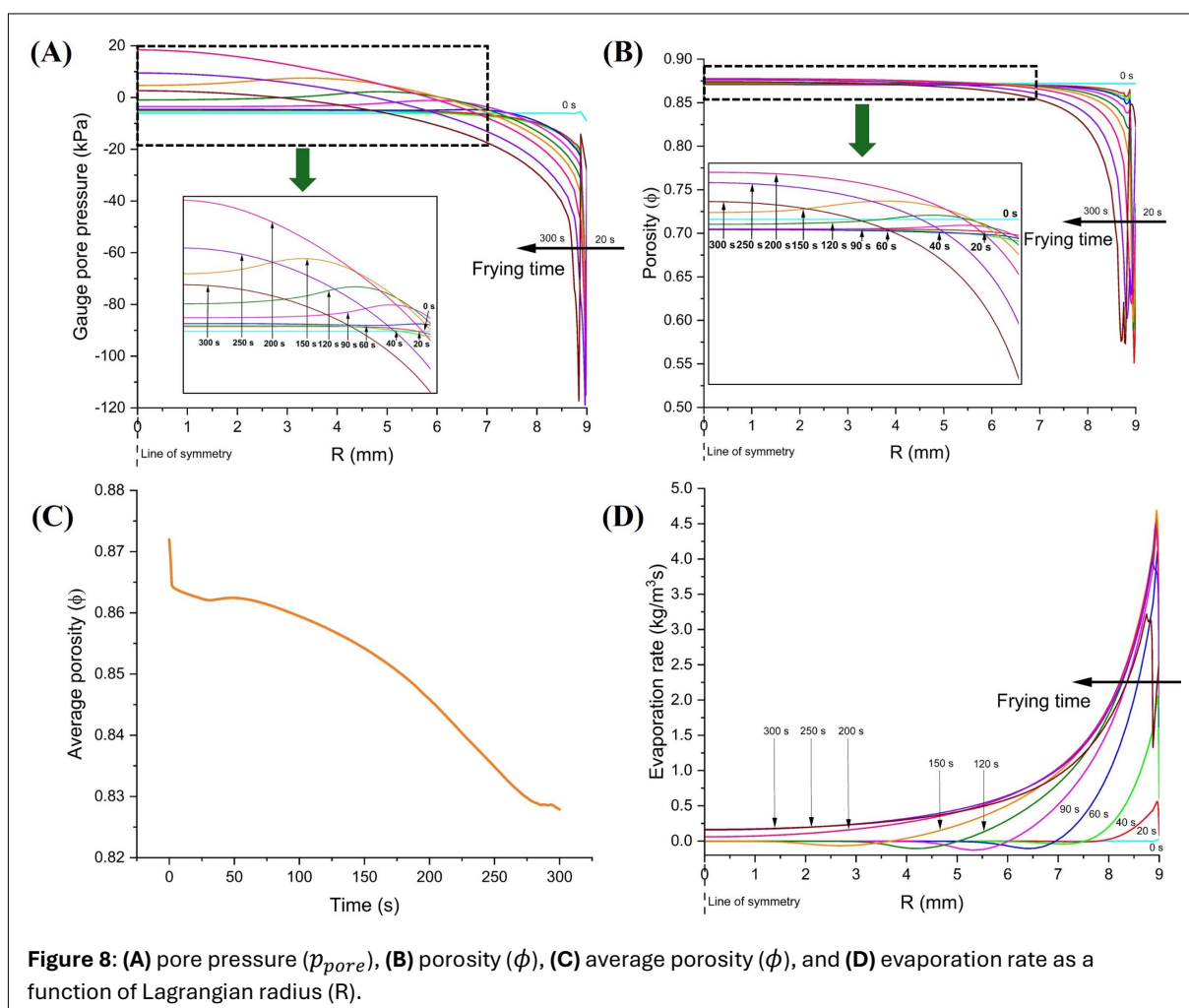


Figure 7: (A) Water phase capillary pressure (p^{cw}) and (B) water pressure (p^w) as a function of Lagrangian radius.

when the pressure in the core is low, there is little opposition to the oil seeping into the surface layers. Thus, a steep increase in oil content is expected. Durán et al. (49) recorded an oil content profile of a similar nature during the early stages of frying of potatoes.

The core temperature remains almost constant initially (Fig. 5A, $t < 50$ s). Heat is transported towards the core by conduction across the porous matrix and by the convection of the fluid phases. While the external heat transfer is fast, the internal heat transfer is comparatively slower. Additionally, the vaporization of water provides a cooling effect, which also prevents the charring of the food (54). As a result, the temperature at the center does not start increasing immediately. This is confirmed by the measured temperature profile (Fig. 5A). The pore pressure at the center shows a similar behavior as its magnitude remains almost unchanged for some time (Fig. 5B, $t < 75$ s). Vitrac et al. (135) recorded similar temperature and pressure trends during the frying of alginate gel cylinders formulated without starch.

The potato samples undergo shrinkage during frying (Fig. 6), and the volume change is rapid, especially when the pore pressure in the core is low. The loss of water from the surface layers leads to high magnitudes of capillary pressure (p^{cw}) (Fig. 7A). Consequently, the water pressure ($p^w = p^g - p^{cw}$) in the surface layers becomes negative (Fig. 7B), and this causes the gauge pore pressure ($p_{pore} = S^w p^w + S^g p^g + S^o p^o$) in the surface layers to become negative (Fig. 8A). Negative gauge pore pressure leads to rapid contraction of the surface layers, and as a result, the porosity near the surface decreases (Fig. 8B). Comparatively, the porosity of the core does not undergo significant changes (Fig. 8B). The average porosity of the sample decreases sharply during the initial stages of frying (Fig. 8C) due to the shrinking surface layers. A decrease in porosity near the surface results in the crunchy crust French fry consumers prefer.



The evaporation rate radial profile (Fig. 8D) illustrates the existence of an evaporation zone instead of a commonly assumed sharp boundary or interface. The evaporation rate has a significant value close to the surface due to the proximity to the frying oil. Evaporation occurs across a region at different rates, referred to as the evaporation zone here, instead of being isolated to a sharp interface within the sample, as confirmed experimentally by Lioumbas and Karapantsios (83). Additionally, the evaporation zone expands with increasing frying time, and the evaporation peak shifts towards the core, which is consistent with the observations of Lioumbas and Karapantsios (83).

After an initial lag, the temperature in the core of the sample begins to rise (Fig. 5A, $t > 50$ s). As the surface temperature rises, the thermal gradient between the bulk oil and the surface of the sample decreases, leading to a decrease in the external convective heat transfer rate. Meanwhile, heat flux into the core is maintained by the thermal gradient between the surface and the core of the sample, causing the core temperature to increase. The temperature profile then peaks and plateaus (Fig. 5A).

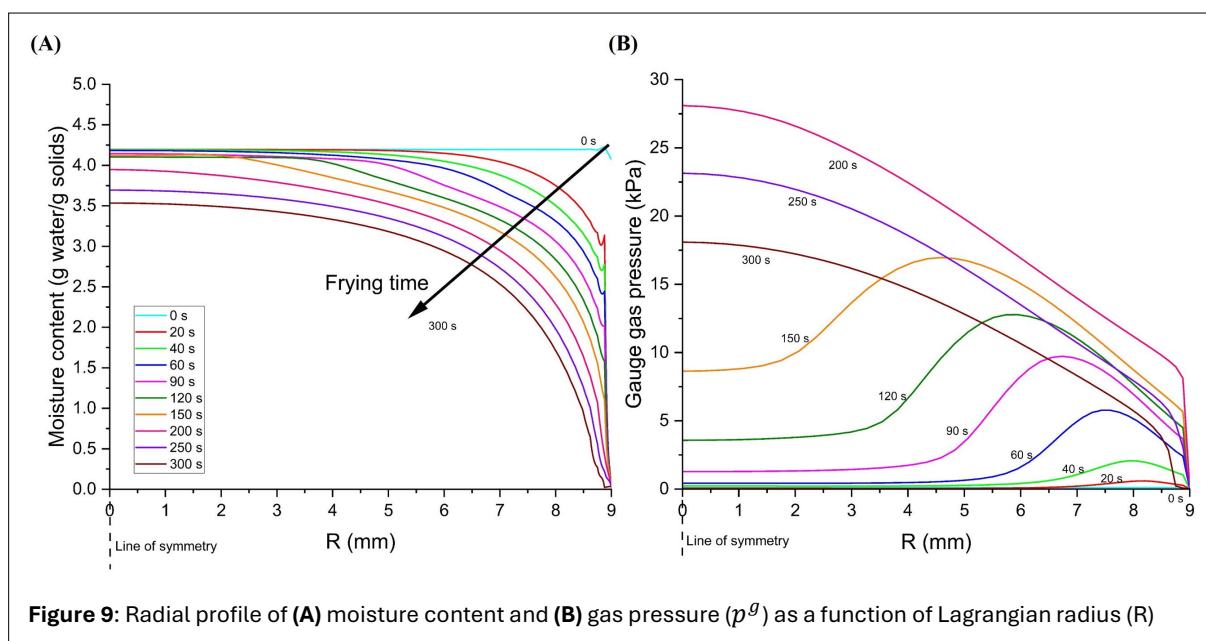


Figure 9: Radial profile of (A) moisture content and (B) gas pressure (p^g) as a function of Lagrangian radius (R)

The water loss from the porous matrix continues, albeit at a slower rate, and a moisture gradient develops across the porous matrix (Fig. 9A). Water from the core, driven by pressure and concentration gradient, moves towards the surface. The internal mass transfer of water is slower than the water loss from the surface, resulting in a moisture gradient.

The gas pressure increases as frying progresses (Fig. 9B). The temperature rise brings about vapor generation and gas expansion in the core of the porous matrix. The gas trapped inside the biopolymeric matrix exerts pressure on the pore walls. With increasing temperature, the gas exerts greater pressure on the pore walls. Additionally, the peak of the gas pressure profile shifts towards the core with increasing frying time (Fig. 9B). This is expected to affect the pore size distribution and pore network development.

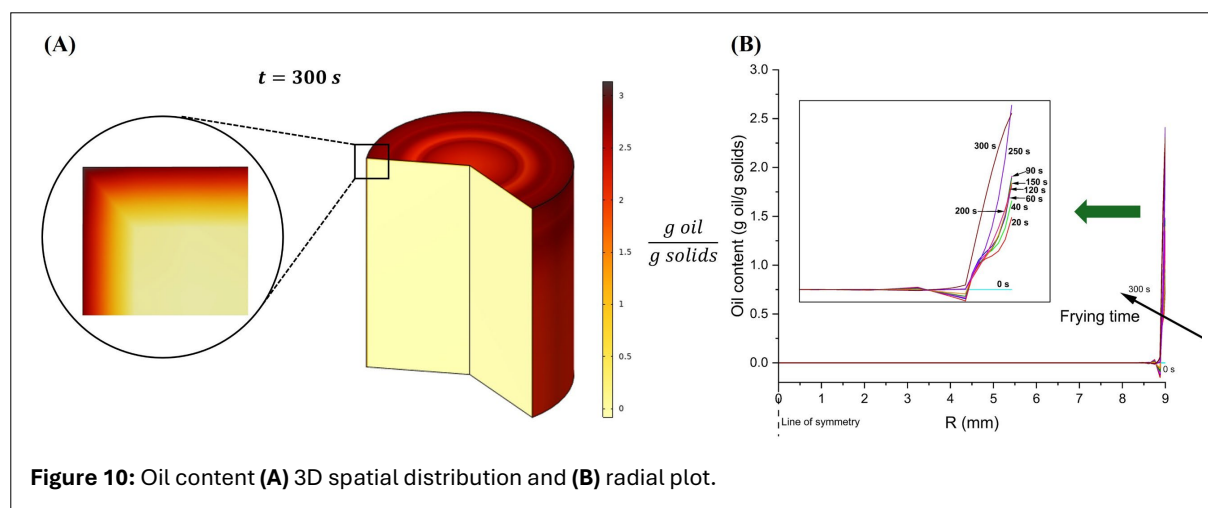
The increase in gas pressure causes the pore pressure to rise (Fig. 5B, $t > 75$ s and Fig. 8A). The absolute pore pressure in the model peaks at 120.49 kPa. The peak pressure, as measured by Shah and Takhar (110), was 134.32 kPa. The model was able to predict the peak pressure during frying reasonably well with a relative difference of 10.30% between the predicted and measured peak pressure values.

The increase in pore pressure in the core (Fig. 5B, Fig. 8A) decreases the shrinkage rate of the potato cylinder (Fig. 6). The negative gauge pore pressure near the surface causes contraction of the matrix, but the increase in pore pressure in the core during the intermediate stages of frying resists the contraction. This slows down the overall rate of shrinkage.

Similarly, after the initial sharp drop in average porosity, its magnitude remains almost constant for a short time and then continues to decrease but at a slower rate (Fig. 8C). Alam and Takhar (8) estimated the porosity changes during the frying of thin potato disks (45 mm diameter and 1.65 mm thickness) using X-ray micro computed tomography (micro-CT) imaging method and also using conventional laboratory techniques like pycnometry. The sample porosity dropped rapidly until a frying time of 20 s was reached, similar to the initial sharp drop in porosity predicted by the current model. The porosity then increased for the remaining frying time (20 – 80 s). The overall percentage change in porosity after 80 s of frying, measured experimentally, was approximately -2.2% (8). The overall change in average porosity predicted by the current model was approximately -5.06% (Fig. 8C).

After the initial rise in oil content, the profile for oil content plateaus (Fig. 4, $t = 50$ to 175 s). The rise in gas pressure and pore pressure in the core of the porous matrix is expected to restrict oil penetration. The plateauing of the oil content profile during the middle stages of frying was also seen by Durán et al. (49) and He et al. (73).

During the immersion phase of frying, a major fraction of the oil remains on the surface while a small fraction enters the porous matrix (Fig. 10A and B). Furthermore, the oil is only able to penetrate the surface layers during immersion frying due to the resistance posed by the increasing pressure inside the porous matrix. This is consistent with the observations of Bouchon and Aguilera (27) and Bouchon et al. (28), using confocal laser scanning microscopy (CLSM).



After reaching a peak, the pore pressure in the core starts to fall (Fig. 5B, $t > 175$ s and Fig. 8A). As water from the core moves outward, water saturation (S^w) in the core decreases. The decrease in water saturation results in an increase in capillary pressure (Fig. 7A) and a subsequent drop in pore pressure in the core. The pore pressure in the core continues to drop until frying is complete. The partial breakdown of the cellular structure and the release of vapors from confined cavities further contribute to this decreasing pressure trend (106).

In the later stages of frying, there is an increase in the oil content (Fig. 4, $t > 175$ s). As pore pressure decreases, the resistance of the food matrix to oil inflow also decreases, which likely contributes to the rise in oil content during the later stages of frying. The oil phase can penetrate the pore spaces that were left empty due to water loss.

As frying approaches completion as well as during the subsequent cooling phase, the porous matrix becomes more susceptible to oil penetration. This could explain the commonly observed increased oil penetration during the cooling phase compared to the immersion phase (28, 73, 86). Understanding these mechanisms can guide further research aimed at optimizing frying techniques. Oil uptake occurs both early in the frying process and in the later stages, including during cooling. By maintaining high pressures in the core of the porous matrix for extended periods, it may be possible to reduce the oil content in fried foods.

4.3. Sensitivity testing

Some material properties are not known with high certainty due to a lack of data availability in the literature, typically because of experimental challenges. Performing sensitivity tests highlights the significance of such properties to the results. Sensitivity tests were performed for water permeability (K^w), oil permeability (K^o), and evaporation rate constant (ζ).

The K^w value was changed by $\pm 10\%$ and $\pm 20\%$ from its base value, and its effect on moisture content, peak pore pressure, and volume change was studied (Fig. 11). The final moisture content was higher for a lower K^w , and lower for a higher K^w .

A higher magnitude of permeability allows faster water loss from the matrix, and as a result, the final moisture content is expected to be lower. Though the effect of varying K^w by $\pm 20\%$ on the moisture content is about $\pm 2\%$, its effect on pore pressure is more significant (Fig. 11). The peak pore pressure at the center rises by 16.83% upon lowering K^w , and drops by 16.09% on raising K^w . When water moves slowly inside the porous matrix for a lower K^w , it results in a higher p^w , and undergoes evaporation and subsequent vapor expansion, generating a higher p^g . The higher pressure is also responsible for lowering the overall shrinkage of the potato samples. As a result, the overall shrinkage reduces for lower K^w values. Conversely, the overall shrinkage increases for higher K^w values.

The oil content of the fried sample increased with an increase in K^o (Fig. 12A). Higher permeability allows faster oil uptake when the conditions are favorable for oil penetration, i.e., when the pressure drops in the core. Conversely, lowering K^o only led to a small drop in oil content.

The effect of varying the evaporation rate constant (ζ) by $\pm 10\%$ and $\pm 20\%$ on the temperature and moisture content of the fried samples was studied (Fig. 12B). The temperature and moisture content are higher for a lower ζ , and are lower for a higher ζ . Increasing ζ leads to faster evaporation, providing

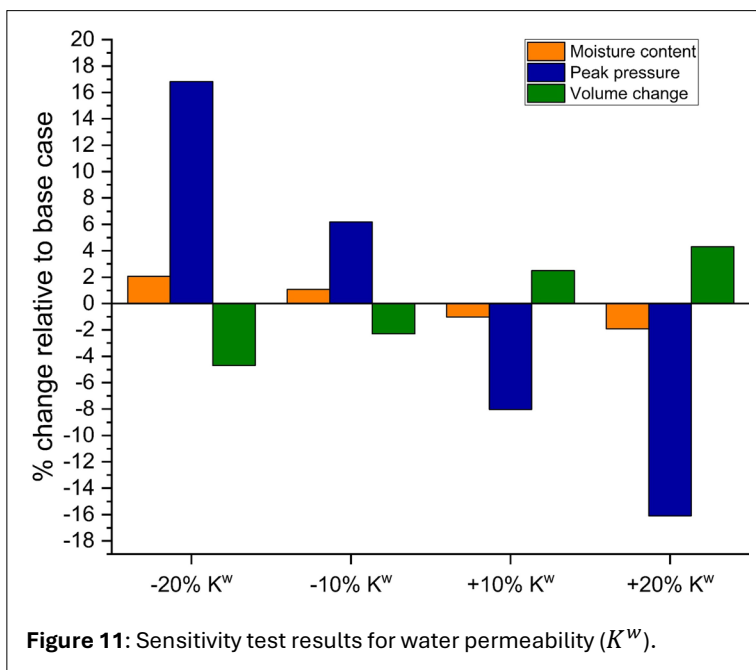


Figure 11: Sensitivity test results for water permeability (K^w).

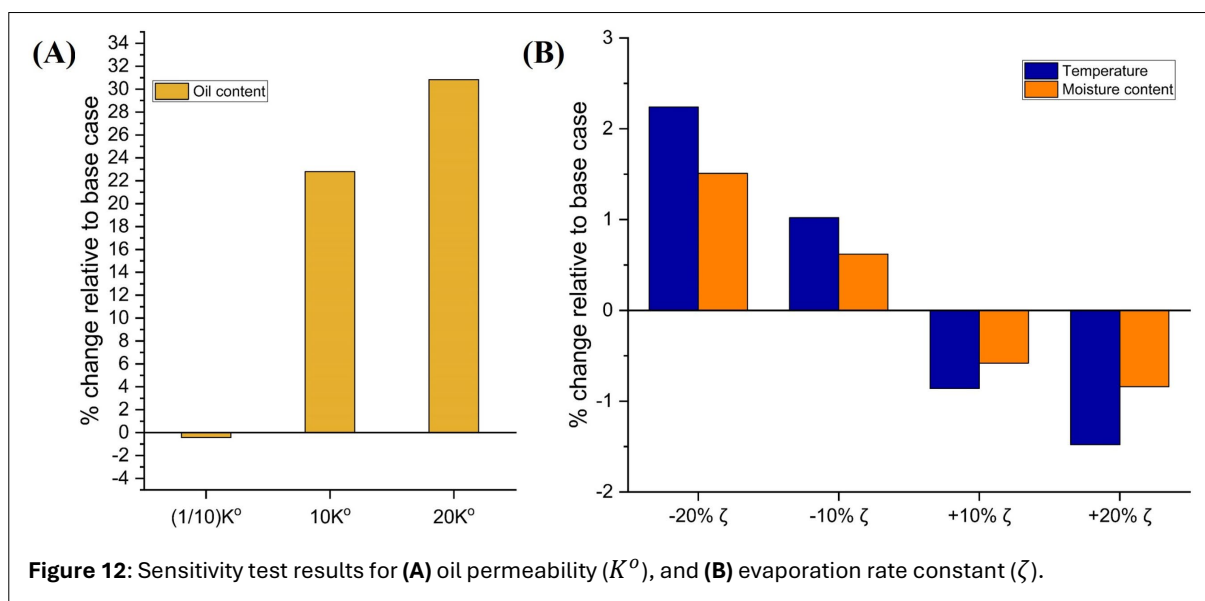


Figure 12: Sensitivity test results for (A) oil permeability (K^o), and (B) evaporation rate constant (ζ).

more evaporative cooling and lowering the temperature. Faster evaporation also contributes to more rapid water loss, as liquid water is converted to vapor and then convected away.

4.4. Limitations of the modeling results

Hybrid-mixture-theory models are based on a rigorously developed porous media transport theory. These models have been successfully applied to soils (24), food gels (6), swelling polymers used in drug delivery applications (137), paperboard (10), wood (85) and different food processes (17, 48, 96, 145). The current study solved the HMT-based unsaturated transport model developed by Takhar (120). However, the reader is made aware of certain limitations related to both model development and solution.

The information lost on upscaling has been noted previously (39, 120). Assumptions like the liquid and solid phase incompressibility, thermodynamic equilibrium between phases, and neglecting gravity-driven fluid flow were made to simplify the model development. These, however, are not prerequisites for developing the model.

Solving mechanistic models for porous biopolymeric matrices like foods is challenging due to the unavailability of appropriate material property data. This is mainly due to experimental difficulties, especially for properties like capillary pressure and permeability. Foods are generally soft and susceptible to structural changes when stress is applied. As discussed in Section 2.8.1 and Section 2.8.2, a pressure-based method is commonly used for estimating capillary pressure and permeability. These techniques were developed for non-cellular and rigid structures like rocks or soils (66). Attempts made to adapt these techniques for foods have faced complications (66, 111). For the current model, we adopted values for material properties based on the little data available in the literature. We have also relied on inverse estimation for properties like the evaporation rate constant. This approach is expected to have some impact on the model solution's accuracy.

The limitations of the experimental properties mentioned are not necessarily weaknesses but rather opportunities for improvement. There is potential for developing new experimental techniques tailored specifically to foods. Large-scale collaborative efforts, involving material scientists and food engineers, are encouraged to address these challenges.

Frying models developed in the past, which may be simplified versions of the currently available models, played a crucial role in guiding advanced model development. Insights gained from these earlier models motivated improvements in model setup and computational techniques, as well as stimulated new experiments. The goal is to continuously update existing models with new data and insights. This work represents another step in that process, aiming to enhance our understanding of frying.

5. CONCLUSIONS

A multiscale porous media model was developed for frying by utilizing the hybrid mixture theory-based unsaturated transport equations. While most previous frying models ignored volume changes to simplify model development, the current model mechanistically predicted the sample deformation using pore pressure as the driving force governing the swelling and shrinking of the porous matrix. The effect of the deforming matrix on the transport processes was accounted for by solving the model in a fully coupled manner. A good agreement was found between model predictions and measured moisture content, oil content, temperature, pressure, and volume changes. While the pressure predicted by previous frying models was either too high or too low compared to the measured pressure, the current model predicted the peak pressure during frying reasonably well. The spatial distribution of different model variables like moisture content, oil content, pressure, and evaporation rate provided more clarity on the different mechanisms involved in frying, and such profiles are challenging to generate experimentally. Internal moisture transport could not keep up with the moisture loss from the surface, and as a result, a moisture gradient developed across the porous matrix. Vaporization and gas expansion at elevated temperatures attained during frying caused the pressure to rise, which restricted the oil

seepage to the peripheral layers of the porous matrix. The evaporation front expanded with frying time, and the peak of the evaporation front moved towards the core. In the final stages of frying, the pressure dropped in the core, making the food matrix more susceptible to oil entry, especially during the cooling phase. Thus, sustaining high pressures in foods for longer times during frying can reduce their oil content. The importance of the model-generated insights for future process optimization studies was discussed. The challenges faced during the model solution, particularly those due to the unavailability of material property data, were highlighted, and further research on devising measurement techniques for soft food materials was encouraged.

NOMENCLATURE

Symbol	Definition
B^α	Mixture viscosity of the biopolymeric matrix (Eq. 3) (Pa. s)
C_p^α	Specific heat of phase α (Eq. 20), $\left(\frac{J}{kgK}\right)$
D^α	Diffusivity of phase α (Eq. 3), $\left(\frac{m^2}{s}\right)$
E	Modulus of elasticity of the biopolymeric matrix (Eq. 3) (Pa)
e	Emissivity (Eq. 34) (dimensionless)
$\beta \hat{e}^\alpha$	Source/sink term (Eq. 1) $\left(\frac{kg}{m^3s}\right)$
h_m^o	Mass transfer coefficient for oil (Eq. 31) $\left(\frac{m}{s}\right)$
h_m^v	Mass transfer coefficient for water vapors (Eq. 33) $\left(\frac{m}{s}\right)$
h_T	Heat transfer coefficient (Eq. 34) $\left(\frac{W}{m^2K}\right)$
K^α	Permeability of phase α (Eq. 3), (m^2)
K_i^g	Intrinsic gas permeability (Eq. 37) (m^2)
K_r^g	Relative gas permeability (Eq. 37) (dimensionless)
K_v	Bulk modulus of the spring in the Maxwell element (Eq. 23) (Pa)
k^α	Thermal conductivity of phase α (Eq. 20), $\left(\frac{W}{mK}\right)$
M^w	Mass fraction of liquid water on a dry basis (Eq. 27) $\left(\frac{g \text{ water}}{g \text{ solids}}\right)$
M_w^v	Molecular weight of water vapors (Eq. 11) $\left(\frac{kg}{mol}\right)$
p^α	Pressure of phase α (Eq. 3), $\left(\frac{N}{m^2}\right)$
$p^{c\alpha}$	Capillary pressure in phase α (Eq. 13), (Pa)
p_{pre}	Pore pressure (Eq. 15) (Pa)
R	Universal gas constant (Eq. 11) $\left(\frac{J}{mol K}\right)$
r	Radial distance (m)
R	Lagrangian radius (m)
S^α	Saturation of phase α in Eulerian coordinates (Eq. 9), (dimensionless)
T	Temperature (Eq. 11) (K)
v^s	Velocity of the solid phase (Eq. 2) $\left(\frac{m}{s}\right)$
$v^{\alpha,s}$	Velocity of α phase with respect to the solid phase (Eq. 1) $\left(\frac{m}{s}\right)$
Greek symbols	Definition
ε^α	Volume fraction of phase α (Eq. 1) (dimensionless)
$\dot{\varepsilon}^\alpha$	Material time derivative of volume fraction of phase α with respect to the solid phase (Eq. 1) (s^{-1})
$\epsilon_{vol,total}$	Total volumetric strain (Eq. 22) (dimensionless)

$\epsilon_{vol,1}$	Volumetric strain in spring (Eq. 22) (dimensionless)
$\epsilon_{vol,2}$	Volumetric strain in dashpot (Eq. 22) (dimensionless)
ζ	Evaporation rate constant (Eq. 12) (s^{-1})
η	Viscosity of the dashpot in the Maxwell element (Eq. 24) ($Pa \cdot s$)
θ	Contact angle ($^\circ$)
λ_v	Latent heat of vaporization (Eq. 20) ($\frac{J}{kg}$)
μ^α	Dynamic viscosity of phase α (Eq. 3), ($Pa \cdot s$)
ρ^α	Density of phase α (Eq. 1), ($\frac{kg}{m^3}$)
ρ_{eq}^v	Equilibrium vapor density (Eq. 12) ($\frac{kg}{m^3}$)
σ	Stefan-Boltzmann constant (Eq. 34) ($\frac{W}{m^2 K^4}$)
σ_{vol}	Volumetric stress (Eq. 25) (Pa)
σ_{pore}	Stress due to pore pressure (Eq. 21) (Pa)
ϕ	Porosity (Eq. 7) (dimensionless)
ω^v	Mass fraction of vapors in the air-vapor mixture (Eq. 6) (dimensionless)
Superscripts	Definition
α	General representation for a phase
β	General representation for a phase
a	Air
g	Gas
o	Oil
v	Vapors
w	Liquid water
Special symbols	Definition
D^s/Dt	Material time derivative with respect to the solid phase (Eq. 1) ($1/s$)
∇_E	Gradient operator in Eulerian coordinates (Eq. 1) ($1/m$)
∇_L	Gradient operator in Lagrangian coordinates (Eq. 1) ($1/m$)

STATEMENTS AND DECLARATIONS

Supplementary Material

An Appendix for this article is available online for [download](#) along with the published article.

Acknowledgements

Thanks to USDA-NIFA for providing financial support under award numbers 2020-67017-31194, ILLU-698-308, and ILLU-698-926.

Author Contributions

Yash Shah contributed to investigation, methodology, software development, validation, and writing of original draft. Pawan Takhar contributed to investigation, software development, funding acquisition, project administration, resources, supervision, and review and editing.

Conflicts of Interest

The authors declare no conflict of interest.

Data, Code & Protocol Availability

Experimental data is available upon request. Computer software used to solve the equations is not being publicly shared.

ORCID IDs

Yash Shah

 <https://orcid.org/0000-0001-5663-6735>

Pawan Singh Takhar

 <https://orcid.org/0000-0002-2617-0767>

REFERENCES

1. Abedi, F., Kumar, S., Kumar, N., Kumar, D., & Takhar, P. S. (2023). Moisture transport and stress development in rice during drying, a Hybrid Mixture Theory-based model. *Drying Technology*, 41(13), 2119–2142. <https://doi.org/10.1080/07373937.2023.2220019>
2. Abedi, F. M., Liu, Y., & Takhar, P. S. (2023). Multiscale modeling of transport mechanisms, strain, and stress in bananas during drying. *Drying Technology*, 1–23. <https://doi.org/10.1080/07373937.2023.2280912>
3. Ablieieva, I., Plyatsuk, L., Roi, I., Chekh, O., Gabbassova, S., Zaitseva, K., & Lutsenko, S. (2021). Study of the oil geopermeation patterns: A case study of ANSYS CFX software application for computer modeling. *Journal of Environmental Management*, 287, 112347. <https://doi.org/10.1016/j.jenvman.2021.112347>
4. Achanta, S. (1995). *Moisture transport in shrinking gels during drying* (Doctoral dissertation, Purdue University).
5. Achanta, S., Cushman, J. H., & Okos, M. R. (1994). On multicomponent, multiphase thermomechanics with interfaces. *International Journal of Engineering Science*, 32(11), 1717–1738. [https://doi.org/10.1016/0020-7225\(94\)90104-X](https://doi.org/10.1016/0020-7225(94)90104-X)
6. Achanta, S., Okos, M. R., Cushman, J. H., & Kessler, D. P. (1997). Moisture transport in shrinking gels during saturated drying. *AIChE Journal*, 43(8), 2112–2122. <https://doi.org/10.1002/aic.690430818>
7. Adedeji, A. A., & Ngadi, M. O. (2011). Microstructural characterization of deep-fat fried breaded chicken nuggets using x-ray micro-computed tomography: Microstructural characterization of chicken nuggets. *Journal of Food Process Engineering*, 34(6), 2205–2219. <https://doi.org/10.1111/j.1745-4530.2009.00565.x>
8. Alam, T., & Takhar, P. S. (2016). Microstructural Characterization of Fried Potato Disks Using X-Ray Micro Computed Tomography. *Journal of Food Science*, 81(3), E651–E664. <https://doi.org/10.1111/1750-3841.13219>
9. Alam, T., Zhao, Y., & Takhar, P. S. (2017). Water and oil permeability of poroelastic potato discs. *International Journal of Food Properties*, 20(3), 633–644. <https://doi.org/10.1080/10942912.2016.1174710>
10. Alexandersson, M., Askfelt, H., & Ristinmaa, M. (2016). Triphasic Model of Heat and Moisture Transport with Internal Mass Exchange in Paperboard. *Transport in Porous Media*, 112(2), 381–408. <https://doi.org/10.1007/s11242-016-0651-9>
11. Alvarez, M. D., Canet, W., Cuesta, F., & Lamua, M. (1998). Viscoelastic characterization of solid foods from creep compliance data: Application to potato tissues. *Zeitschrift Für Lebensmitteluntersuchung Und -Forschung A*, 207(5), 356–362. <https://doi.org/10.1007/s002170050345>
12. Amestoy, P., Buttari, A., Duff, I., Guermouche, A., L'Excellent, J.-Y., & Uçar, B. (2011). Mumps. In D. Padua (Ed.), *Encyclopedia of Parallel Computing* (pp. 1232–1238). Springer US. https://doi.org/10.1007/978-0-387-09766-4_204
13. Antunes-Rohling, A., Ciudad-Hidalgo, S., Mir-Bel, J., Raso, J., Cebrián, G., & Álvarez, I. (2018). Ultrasound as a pretreatment to reduce acrylamide formation in fried potatoes. *Innovative Food Science & Emerging Technologies*, 49, 158–169. <https://doi.org/10.1016/j.ifset.2018.08.010>
14. Asokapandian, S., Swamy, G. J., & Hajjul, H. (2020). Deep fat frying of foods: A critical review on process and product parameters. *Critical Reviews in Food Science and Nutrition*, 60(20), 3400–3413. <https://doi.org/10.1080/10408398.2019.1688761>
15. Ateba, P., & Mittal, G. S. (1994). Modelling the deep-fat frying of beef meatballs. *International Journal of Food Science & Technology*, 29(4), 429–440. <https://doi.org/10.1111/j.1365-2621.1994.tb02084.x>
16. Balaban, M. (1990). Effect of volume change in foods on the temperature and moisture content predictions of simultaneous heat and moisture transfer models. *Journal of Food Process Engineering*, 12(1), 67–88. <https://doi.org/10.1111/j.1745-4530.1990.tb00041.x>
17. Bansal, H. S., Takhar, P. S., Alvarado, C. Z., & Thompson, L. D. (2015). Transport Mechanisms and Quality Changes During Frying of Chicken Nuggets – Hybrid Mixture Theory Based Modeling and Experimental Verification. *Journal of Food Science*, 80(12), E2759–E2773. <https://doi.org/10.1111/1750-3841.13082>
18. Bansal, H. S., Takhar, P. S., & Maneerote, J. (2014). Modeling multiscale transport mechanisms, phase changes and thermomechanics during frying. *Food Research International*, 62, 709–717. <https://doi.org/10.1016/j.foodres.2014.04.016>
19. Bassama, J., Brat, P., Boulanger, R., Günata, Z., & Bohuon, P. (2012). Modeling deep-fat frying for control of acrylamide reaction in plantain. *Journal of Food Engineering*, 113(1), 156–166. <https://doi.org/10.1016/j.jfoodeng.2012.04.004>

20. Battiato, I., Ferrero V, P. T., O' Malley, D., Miller, C. T., Takhar, P. S., Valdés-Parada, F. J., & Wood, B. D. (2019). Theory and Applications of Macroscale Models in Porous Media. *Transport in Porous Media*, 130(1), 5–76. <https://doi.org/10.1007/s11242-019-01282-2>
21. Bennethum, L. S., & Cushman, J. H. (1996a). Multiscale, hybrid mixture theory for swelling systems—I: Balance laws. *International Journal of Engineering Science*, 34(2), 125–145. [https://doi.org/10.1016/0020-7225\(95\)00089-5](https://doi.org/10.1016/0020-7225(95)00089-5)
22. Bennethum, L. S., & Cushman, J. H. (1996b). Multiscale, hybrid mixture theory for swelling systems—II: Constitutive theory. *International Journal of Engineering Science*, 34(2), 147–169. [https://doi.org/10.1016/0020-7225\(95\)00090-9](https://doi.org/10.1016/0020-7225(95)00090-9)
23. Bennethum, L. S., & Cushman, J. H. (1999). Coupled solvent and heat transport of a mixture of swelling porous particles and fluids: Single time-scale problem. *Transport in Porous Media*, 36, 211–244. <https://doi.org/10.1023/A:1006534302277>
24. Bennethum, L. S., Murad, M. A., & Cushman, J. H. (1997). Modified Darcy's law, Terzaghi's effective stress principle and Fick's law for swelling clay soils. *Computers and Geotechnics*, 20(3–4), 245–266. [https://doi.org/10.1016/S0266-352X\(97\)00005-0](https://doi.org/10.1016/S0266-352X(97)00005-0)
25. Bird, R. B., Stewart, W. E., & Lightfoot, E. N. (2002). *Transport phenomena* (2nd, Wiley international ed ed.). J. Wiley.
26. Bonneau, P., & Puiggali, J.-R. (1993). Influence of heartwood-sapwood proportions on the drying kinetics of a board. *Wood Science and Technology*, 28(1). <https://doi.org/10.1007/BF00193878>
27. Bouchon, P., & Aguilera, J. M. (2001). Microstructural analysis of frying potatoes. *International Journal of Food Science and Technology*, 36(6), 669–676. <https://doi.org/10.1046/j.1365-2621.2001.00499.x>
28. Bouchon, P., Aguilera, J., & Pyle, D. (2003). Structure oil-absorption relationships during deep-fat frying. *Journal of Food Science*, 68(9), 2711–2716. <https://doi.org/10.1111/j.1365-2621.2003.tb05793.x>
29. Bouchon, P., Hollins, P., Pearson, M., Pyle, D. L., & Tobin, M. J. (2001). Oil Distribution in Fried Potatoes Monitored by Infrared Microspectroscopy. *Journal of Food Science*, 66(7), 918–923. <https://doi.org/10.1111/j.1365-2621.2001.tb08212.x>
30. Bowen, R. M. (1980). Incompressible porous media models by use of the theory of mixtures. *International Journal of Engineering Science*, 18(9), 1129–1148. [https://doi.org/10.1016/0020-7225\(80\)90114-7](https://doi.org/10.1016/0020-7225(80)90114-7)
31. Bradford, S. A., & Leij, F. J. (1996). Predicting Two- and Three-Fluid Capillary Pressure-Saturation Relationships of Porous Media With Fractional Wettability. *Water Resources Research*, 32(2), 251–259. <https://doi.org/10.1029/95WR03239>
32. Cahill, L. E., Pan, A., Chiuvè, S. E., Sun, Q., Willett, W. C., Hu, F. B., & Rimm, E. B. (2014). Fried-food consumption and risk of type 2 diabetes and coronary artery disease: A prospective study in 2 cohorts of US women and men. *The American Journal of Clinical Nutrition*, 100(2), 667–675. <https://doi.org/10.3945/ajcn.114.084129>
33. Cazzaniga, A., Brousse, M. M., & Linares, A. R. (2022). Kinetics of moisture loss applied to the baking of snacks with pregelatinized cassava starch. *Journal of Food Science*, 87(6), 2651–2662. <https://doi.org/10.1111/1750-3841.16188>
34. Cengel, Y. A., Boles, M. A., & Kanoğlu, M. (2011). *Thermodynamics: An engineering approach* (Vol. 5). McGraw-Hill New York.
35. Chen, Y., & Moreira, R. G. (1997). Modelling of a Batch Deep-Fat Frying Process for Tortilla Chips. *Food and Bioproducts Processing*, 75(3), 181–190. <https://doi.org/10.1205/096030897531531>
36. Choe, E., & Min, D. B. (2007). Chemistry of Deep-Fat Frying Oils. *Journal of Food Science*, 72(5), R77–R86. <https://doi.org/10.1111/j.1750-3841.2007.00352.x>
37. Coleman, B. D., & Noll, W. (1963). The thermodynamics of elastic materials with heat conduction and viscosity. *Archive for Rational Mechanics and Analysis*, 13(1), 167–178. <https://doi.org/10.1007/BF01262690>
38. Corraera, S., Fasano, A., Fusi, L., & Primicerio, M. (2007). Modelling wax diffusion in crude oils: The cold finger device. *Applied Mathematical Modelling*, 31(10), 2286–2298. <https://doi.org/10.1016/j.apm.2006.09.007>
39. Cushman, J. H., Bennethum, L. S., & Hu, B. X. (2002). A primer on upscaling tools for porous media. *Advances in Water Resources*, 25(8–12), 1043–1067. [https://doi.org/10.1016/S0309-1708\(02\)00047-7](https://doi.org/10.1016/S0309-1708(02)00047-7)
40. Dadmohammadi, Y., Kantzas, A., Yu, X., & Datta, A. K. (2020). Estimating permeability and porosity of plant tissues: Evolution from raw to the processed states of potato. *Journal of Food Engineering*, 277, 109912. <https://doi.org/10.1016/j.jfoodeng.2020.109912>
41. Daher, F. B., & Braybrook, S. A. (2015). How to let go: Pectin and plant cell adhesion. *Frontiers in Plant Science*, 6. <https://doi.org/10.3389/fpls.2015.00523>
42. Dash, K. K., Sharma, M., & Tiwari, A. (2022). Heat and mass transfer modeling and quality changes during deep fat frying: A comprehensive review. *Journal of Food Process Engineering*, 45(4). <https://doi.org/10.1111/jfpe.13999>
43. Datta, A. K. (2006). Hydraulic Permeability of Food Tissues. *International Journal of Food Properties*, 9(4), 767–780. <https://doi.org/10.1080/10942910600596167>

44. Datta, A. K. (2007a). Porous media approaches to studying simultaneous heat and mass transfer in food processes. I: Problem formulations. *Journal of Food Engineering*, 80(1), 80–95. <https://doi.org/10.1016/j.jfoodeng.2006.05.013>
45. Datta, A. K. (2007b). Porous media approaches to studying simultaneous heat and mass transfer in food processes. II: Property data and representative results. *Journal of Food Engineering*, 80(1), 96–110. <https://doi.org/10.1016/j.jfoodeng.2006.05.012>
46. Dehghan Nasiri, Fereshteh., Mohebbi, Mohebbat., Tabatabaee Yazdi, Farideh., & Haddad Khodaparast, M. Hossein. (2011). Kinetic modeling of mass transfer during deep fat frying of shrimp nugget prepared without a pre-frying step. *Food and Bioproducts Processing*, 89(3), 241–247. <https://doi.org/10.1016/j.fbp.2010.11.009>
47. Dhall, A., & Datta, A. K. (2011). Transport in deformable food materials: A poromechanics approach. *Chemical Engineering Science*, 66(24), 6482–6497. <https://doi.org/10.1016/j.ces.2011.09.001>
48. Ditudompo, S., & Takhar, P. S. (2015). Hybrid mixture theory based modeling of transport mechanisms and expansion-thermomechanics of starch during extrusion. *AIChE Journal*, 61(12), 4517–4532. <https://doi.org/10.1002/aic.14936>
49. Durán, M., Pedreschi, F., Moyano, P., & Troncoso, E. (2007). Oil partition in pre-treated potato slices during frying and cooling. *Journal of Food Engineering*, 81(1), 257–265. <https://doi.org/10.1016/j.jfoodeng.2006.11.004>
50. Eckert, E. R., & Drake Jr, R. M. (1987). *Analysis of heat and mass transfer*.
51. E. E. Finney & Jr. And C. W. Hall. (1967). Elastic Properties of Potatoes. *Transactions of the ASAE*, 10(1), 0004–0008. <https://doi.org/10.13031/2013.39578>
52. Ehlers, W., & Bluhm, J. (Eds.). (2002). *Porous Media*. Springer Berlin Heidelberg. <https://doi.org/10.1007/978-3-662-04999-0>
53. Ehlers, W., & Markert, B. (2000). On the viscoelastic behaviour of fluid-saturated porous materials. *Granular Matter*, 2(3), 153–161. <https://doi.org/10.1007/s100359900037>
54. Erickson, M. D. (Ed.). (2007). *Deep frying: Chemistry, nutrition, and practical applications* (2nd ed). AOCS Press.
55. Esteban, B., Riba, J.-R., Baquero, G., Rius, A., & Puig, R. (2012). Temperature dependence of density and viscosity of vegetable oils. *Biomass and Bioenergy*, 42, 164–171. <https://doi.org/10.1016/j.biombioe.2012.03.007>
56. Esveld, D. C., Van Der Sman, R. G. M., Van Dalen, G., Van Duynhoven, J. P. M., & Meinders, M. B. J. (2012). Effect of morphology on water sorption in cellular solid foods. Part I: Pore scale network model. *Journal of Food Engineering*, 109(2), 301–310. <https://doi.org/10.1016/j.jfoodeng.2011.08.016>
57. Fang, Y., & Li, B. (2016). Multiscale problems and analysis of soil mechanics. *Mechanics of Materials*, 103, 55–67. <https://doi.org/10.1016/j.mechmat.2016.09.003>
58. Farinu, A., & Baik, O.-D. (2007). Heat transfer coefficients during deep fat frying of sweetpotato: Effects of product size and oil temperature. *Food Research International*, 40(8), 989–994. <https://doi.org/10.1016/j.foodres.2007.05.006>
59. Farkas, B. E., Singh, R. P., & Rumsey, T. R. (1996a). Modeling heat and mass transfer in immersion frying. I, model development. *Journal of Food Engineering*, 29(2), 211–226. [https://doi.org/10.1016/0260-8774\(95\)00072-0](https://doi.org/10.1016/0260-8774(95)00072-0)
60. Farkas, B. E., Singh, R. P., & Rumsey, T. R. (1996b). Modeling heat and mass transfer in immersion frying. II, model solution and verification. *Journal of Food Engineering*, 29(2), 227–248. [https://doi.org/10.1016/0260-8774\(95\)00048-8](https://doi.org/10.1016/0260-8774(95)00048-8)
61. Feng, H., Tang, J., Plumb, O. A., & Cavaliere, R. P. (2004). Intrinsic and relative permeability for flow of humid air in unsaturated apple tissues. *Journal of Food Engineering*, 62(2), 185–192. [https://doi.org/10.1016/S0260-8774\(03\)00231-0](https://doi.org/10.1016/S0260-8774(03)00231-0)
62. Gadiraju, T., Patel, Y., Gaziano, J., & Djoussé, L. (2015). Fried Food Consumption and Cardiovascular Health: A Review of Current Evidence. *Nutrients*, 7(10), 8424–8430. <https://doi.org/10.3390/nu7105404>
63. Gamble, M., Rice, P., & Selman, J. (1987). Relationship between oil uptake and moisture loss during frying of potato slices from cv Record UK tubers. *International Journal of Food Science & Technology*, 22(3), 233–241. <https://doi.org/10.1111/j.1365-2621.1987.tb00483.x>
64. G. Gray, W., & A. Schrefler, B. (2007). Analysis of the solid phase stress tensor in multiphase porous media. *International Journal for Numerical and Analytical Methods in Geomechanics*, 31(4), 541–581. <https://doi.org/10.1002/nag.541>
65. Gulati, T., Zhu, H., & Datta, A. K. (2016). Coupled electromagnetics, multiphase transport and large deformation model for microwave drying. *Chemical Engineering Science*, 156, 206–228. <https://doi.org/10.1016/j.ces.2016.09.004>
66. Halder, A., Datta, A. K., & Spanswick, R. M. (2011). Water transport in cellular tissues during thermal processing. *AIChE Journal*, 57(9), 2574–2588. <https://doi.org/10.1002/aic.12465>

67. Halder, A., Dhall, A., & Datta, A. K. (2007a). An Improved, Easily Implementable, Porous Media Based Model for Deep-Fat Frying. *Food and Bioproducts Processing*, 85(3), 209–219. <https://doi.org/10.1205/fbp07033>
68. Halder, A., Dhall, A., & Datta, A. K. (2007b). An Improved, Easily Implementable, Porous Media Based Model for Deep-Fat Frying. *Food and Bioproducts Processing*, 85(3), 220–230. <https://doi.org/10.1205/fbp07034>
69. Hassanizadeh, M., & Gray, W. G. (1979a). General conservation equations for multi-phase systems: 1. Averaging procedure. *Advances in Water Resources*, 2, 131–144. [https://doi.org/10.1016/0309-1708\(79\)90025-3](https://doi.org/10.1016/0309-1708(79)90025-3)
70. Hassanizadeh, M., & Gray, W. G. (1979b). General conservation equations for multi-phase systems: 2. Mass, momenta, energy, and entropy equations. *Advances in Water Resources*, 2, 191–203. [https://doi.org/10.1016/0309-1708\(79\)90035-6](https://doi.org/10.1016/0309-1708(79)90035-6)
71. Hassanizadeh, M., & Gray, W. G. (1980). General conservation equations for multi-phase systems: 3. Constitutive theory for porous media flow. *Advances in Water Resources*, 3(1), 25–40. [https://doi.org/10.1016/0309-1708\(80\)90016-0](https://doi.org/10.1016/0309-1708(80)90016-0)
72. Hayek, M. (2017). A Model for Subsurface Oil Pollutant Migration. *Transport in Porous Media*, 120(2), 373–393. <https://doi.org/10.1007/s11242-017-0926-9>
73. He, D.-B., Xu, F., Hua, T.-C., & Song, X.-Y. (2013). Oil absorption mechanism of fried food during cooling process: Mechanism and reduction of oil uptake in fried potato. *Journal of Food Process Engineering*, 36(4), 412–417. <https://doi.org/10.1111/j.1745-4530.2012.00681.x>
74. Ho, Q. T., Verboven, P., Fanta, S. W., Abera, M. K., Retta, M. A., Herremans, E., Defraeye, T., & Nicolai, B. M. (2014). A Multiphase Pore Scale Network Model of Gas Exchange in Apple Fruit. *Food and Bioprocess Technology*, 7(2), 482–495. <https://doi.org/10.1007/s11947-012-1043-y>
75. Hubbard, L. J., & Farkas, B. E. (1999). A method for determining the convective heat transfer coefficient during immersion frying. *Journal of Food Process Engineering*, 22(3), 201–214. <https://doi.org/10.1111/j.1745-4530.1999.tb00481.x>
76. Incropera, F. P., DeWitt, D. P., Bergman, T. L., & Lavine, A. S. (1996). *Fundamentals of heat and mass transfer* (Vol. 6). Wiley New York.
77. Johnson, C. (2012). Numerical solution of partial differential equations by the finite element method. Courier Corporation.
78. Kang, W., & Chung, W. Y. (2009). Liquid water diffusivity of wood from the capillary pressure-moisture relation. *Journal of Wood Science*, 55(2), 91–99. <https://doi.org/10.1007/s10086-008-1009-x>
79. Khosravi, M., & Azizian, S. (2016). A new kinetic model for absorption of oil spill by porous materials. *Microporous and Mesoporous Materials*, 230, 25–29. <https://doi.org/10.1016/j.micromeso.2016.04.039>
80. Kita, A., Lisińska, G., & Gołubowska, G. (2007). The effects of oils and frying temperatures on the texture and fat content of potato crisps. *Food Chemistry*, 102(1), 1–5. <https://doi.org/10.1016/j.foodchem.2005.08.038>
81. Krokida, M. K., Oreopoulou, V., Maroulis, Z. B., & Marinos-Kouris, D. (2001). Colour changes during deep fat frying. *Journal of Food Engineering*, 48(3), 219–225. [https://doi.org/10.1016/S0260-8774\(00\)00161-8](https://doi.org/10.1016/S0260-8774(00)00161-8)
82. Liang, B., Lan, H., & Lin, N. (2018). Diffusion simulation and safety assessment of oil leaked in the ground. *Journal of Petroleum Science and Engineering*, 167, 498–505. <https://doi.org/10.1016/j.petrol.2018.04.034>
83. Lioumbas, J. S., & Karapantsios, T. D. (2012). Evaporation Front Compared with Crust Thickness in Potato Deep-Fat Frying. *Journal of Food Science*, 77(1), E17–E25. <https://doi.org/10.1111/j.1750-3841.2011.02472.x>
84. Liu, Y., Zhu, W., Luo, L., Li, X., & Yu, H. (2014). A Mathematical Model for Vacuum Far-Infrared Drying of Potato Slices. *Drying Technology*, 32(2), 180–189. <https://doi.org/10.1080/07373937.2013.811687>
85. Mmari, W., & Johannesson, B. (2020). Modeling transient and hysteretic hygrothermal processes in wood using the hybrid mixture theory. *International Journal of Heat and Mass Transfer*, 163, 120408. <https://doi.org/10.1016/j.ijheatmasstransfer.2020.120408>
86. Moreira, R. G., Sun, X., & Chen, Y. (1997). Factors affecting oil uptake in tortilla chips in deep-fat frying. *Journal of Food Engineering*, 31(4), 485–498. [https://doi.org/10.1016/S0260-8774\(96\)00088-X](https://doi.org/10.1016/S0260-8774(96)00088-X)
87. Murad, M. A., Bennethum, L. S., & Cushman, J. H. (1995). A multi-scale theory of swelling porous media: I. Application to one-dimensional consolidation. *Transport in Porous Media*, 19(2), 93–122. <https://doi.org/10.1007/BF00626661>
88. Naghavi, E.-A., Dehghannya, J., & Ghanbarzadeh, B. (2018). 3D computational simulation for the prediction of coupled momentum, heat and mass transfer during deep-fat frying of potato strips coated with different concentrations of alginate. *Journal of Food Engineering*, 235, 64–78. <https://doi.org/10.1016/j.jfoodeng.2018.04.026>
89. Narasimhan, T. N., Houston, W. N., & Nur, A. M. (1980). The role of pore pressure in deformation in geologic processes. *Geology*, 8(7), 349. [https://doi.org/10.1130/0091-7613\(1980\)8<349:TROPPI>2.0.CO;2](https://doi.org/10.1130/0091-7613(1980)8<349:TROPPI>2.0.CO;2)
90. Neethu, K., Franklin, M. E. E., Pushpadass, H. A., Menon, R. R., Rao, K. J., & Nath, B. S. (2015). Analysis of Transient Heat and Mass Transfer during Deep-Fat Frying of *Pantofa*. Heat and Mass Transfer during Frying of *Pantofa*. *Journal of Food Processing and Preservation*, 39(6), 966–977. <https://doi.org/10.1111/jfpp.12310>

91. Nellis, G., & Klein, S. (2008). *Heat transfer*. Cambridge University Press.
92. Ni, H. (1997). Multiphase moisture transport in porous media under intensive microwave heating. Faculty of the Graduate School of Cornell University. OCLC Number / Unique Identifier:781645578. <https://search.worldcat.org/title/multiphase-moisture-transport-in-porous-media-under-intensive-microwave-heating/oclc/781645578?referer=di&ht=edition>
93. Ni, H., & Datta, A. K. (1999). Moisture, Oil and Energy Transport During Deep-Fat Frying of Food Materials. *Food and Bioproducts Processing*, 77(3), 194–204. <https://doi.org/10.1205/096030899532475>
94. Nield, D. A., & Bejan, A. (2006). *Convection in porous media* (3rd ed). Springer.
95. Oghenejoboh, K., & Puyate, Y. (2010). Experimental investigation of the effects of crude oil physical properties on its diffusion rate in soil medium. *I Control Pollution*, 26(2). <https://www.icontrolpollution.com/peer-reviewed/experimental-investigation-of-the-effects-of-crude-oil-physical-properties-on-its-diffusion-rate-in-soil-medium-45530.html>
96. Ozturk, O. K., & Takhar, P. S. (2021). Hybrid mixture theory-based modeling of moisture transport coupled with quality changes in strawberries and carrots. *Drying Technology*, 39(7), 932–949. <https://doi.org/10.1080/07373937.2020.1733005>
97. Park, S., Venditti, R. A., Jameel, H., & Pawlak, J. J. (2007). Studies of the heat of vaporization of water associated with cellulose fibers characterized by thermal analysis. *Cellulose*, 14(3), 195–204. <https://doi.org/10.1007/s10570-007-9108-1>
98. Patsioura, A., Vauvre, J.-M., Kesteloot, R., Jamme, F., Hume, P., & Vitrac, O. (2015). Microscopic imaging of biphasic oil-air flow in French fries using synchrotron radiation. *AIChE Journal*, 61(4), 1427–1446. <https://doi.org/10.1002/aic.14744>
99. Patsioura, A., Vauvre, J.-M., Kesteloot, R., Smith, P., Trystram, G., & Vitrac, O. (2016). Mechanisms of Oil Uptake in French Fries. In *Advances in Potato Chemistry and Technology* (pp. 503–526). Elsevier. <https://doi.org/10.1016/B978-0-12-800002-1.00017-0>
100. Perry, R. H., & Green, D. W. (1997). Perry's Chemical Engineers' Handbook 7th edition (1997). ISBN-13, 978–0071834087.
101. Pinthus, E. J., & Saguy, I. (1994). Initial Interfacial Tension and Oil Uptake by Deep-fat Fried Foods. *Journal of Food Science*, 59(4), 804–807. <https://doi.org/10.1111/j.1365-2621.1994.tb08132.x>
102. Qu, Z., An, C., Mei, Z., Yue, R., Zhao, S., Feng, Q., Cai, M., & Wen, J. (2022). An experimental and modeling study on the penetration of spilled oil into thawing frozen soil. *Environmental Science: Processes & Impacts*, 24(12), 2398–2408. <https://doi.org/10.1039/D2EM00368F>
103. Rice, J. D., & Duncan, J. M. (2010). Deformation and Cracking of Seepage Barriers in Dams due to Changes in the Pore Pressure Regime. *Journal of Geotechnical and Geoenvironmental Engineering*, 136(1), 16–25. [https://doi.org/10.1061/\(ASCE\)GT.1943-5606.0000241](https://doi.org/10.1061/(ASCE)GT.1943-5606.0000241)
104. Rifai, L., & Saleh, F. A. (2020). A Review on Acrylamide in Food: Occurrence, Toxicity, and Mitigation Strategies. *International Journal of Toxicology*, 39(2), 93–102. <https://doi.org/10.1177/1091581820902405>
105. Sahin, S., & Sumnu, S. G. (Eds.). (2009). *Advances in deep-fat frying of foods*. CRC Press.
106. Sandhu, J. S., Bansal, H., & Takhar, P. S. (2013). Experimental measurement of physical pressure in foods during frying. *Journal of Food Engineering*, 115(2), 272–277. <https://doi.org/10.1016/j.jfoodeng.2012.10.016>
107. Sandhu, J. S., & Takhar, P. S. (2015). Effect of frying parameters on mechanical properties and microstructure of potato disks. *Journal of Texture Studies*, 46(5), 385–397. <https://doi.org/10.1111/jtxs.12138>
108. Sandhu, J. S., & Takhar, P. S. (2018). Verification of hybrid mixture theory based two-scale unsaturated transport processes using controlled frying experiments. *Food and Bioproducts Processing*, 110, 26–39. <https://doi.org/10.1016/j.fbp.2018.04.004>
109. Sasahara, K., & Sakai, N. (2014). Development of shear deformation due to the increase of pore pressure in a sandy model slope during rainfall. *Engineering Geology*, 170, 43–51. <https://doi.org/10.1016/j.enggeo.2013.12.005>
110. Shah, Y., & Takhar, P. S. (2022). Pressure development and volume changes during frying and post-frying of potatoes. *LWT*, 172, 114243. <https://doi.org/10.1016/j.lwt.2022.114243>
111. Shah, Y., & Takhar, P. S. (2023). Capillary Pressure in Unsaturated Food Systems: Its Importance and Accounting for It in Mathematical Models. *Food Engineering Reviews*. <https://doi.org/10.1007/s12393-023-09341-7>
112. Shivhare, U. S., Raghavan, G. S. V., & Bosisio, R. G. (1994). Modelling the Drying Kinetics of Maize in a Microwave Environment. *Journal of Agricultural Engineering Research*, 57(3), 199–205. <https://doi.org/10.1006/jaer.1994.1019>
113. Singh, F., Katiyar, V. K., & Singh, B. P. (2015). Mathematical modeling to study influence of porosity on apple and potato during dehydration. *Journal of Food Science and Technology*, 52(9), 5442–5455. <https://doi.org/10.1007/s13197-014-1647-5>

114. Singh, P. P., Cushman, J. H., & Maier, D. E. (2003). Three scale thermomechanical theory for swelling biopolymeric systems. *Chemical Engineering Science*, 58(17), 4017–4035. [https://doi.org/10.1016/S0009-2509\(03\)00283-5](https://doi.org/10.1016/S0009-2509(03)00283-5)
115. Singh, P. P., Cushman, J. N., Bennethum, L. S., & Maier, D. E. (2003). Thermomechanics of swelling biopolymeric systems. *Transport in Porous Media*, 53, 1–24. <https://doi.org/10.1023/A:1023515101436>
116. Singh, P. P., Maier, D. E., Cushman, J. H., & Campanella, O. H. (2004). Effect of viscoelastic relaxation on moisture transport in foods. Part II: Sorption and drying of soybeans. *Journal of Mathematical Biology*, 49(1). <https://doi.org/10.1007/s00285-003-0250-6>
117. Singh, P. P., Maier, D. E., Cushman, J. H., Haghghi, K., & Corvalan, C. (2004). Effect of viscoelastic relaxation on moisture transport in foods. Part I: Solution of general transport equation. *Journal of Mathematical Biology*, 49(1). <https://doi.org/10.1007/s00285-003-0249-z>
118. Steffe, J. F. (1996). *Rheological methods in food process engineering*. Freeman Press.
119. Takhar, P. S. (2011). Hybrid mixture theory based moisture transport and stress development in corn kernels during drying: Coupled fluid transport and stress equations. *Journal of Food Engineering*, 105(4), 663–670. <https://doi.org/10.1016/j.jfoodeng.2011.03.033>
120. Takhar, P. S. (2014). Unsaturated fluid transport in swelling poroviscoelastic biopolymers. *Chemical Engineering Science*, 109, 98–110. <https://doi.org/10.1016/j.ces.2014.01.016>
121. Takhar, P. S., Maier, D. E., Campanella, O. H., & Chen, G. (2011). Hybrid mixture theory based moisture transport and stress development in corn kernels during drying: Validation and simulation results. *Journal of Food Engineering*, 106(4), 275–282. <https://doi.org/10.1016/j.jfoodeng.2011.05.006>
122. Tan, L., Yuan, Y., Zhao, Z., Xu, Y., & Yuan, Y. (2023). Insights in mechanism of drying shrinkage by pore-scale modeling of heat-moisture and stress-strain distribution for high-moisture porous media. *International Journal of Thermal Sciences*, 188, 108226. <https://doi.org/10.1016/j.ijthermalsci.2023.108226>
123. Tang, Y., Valocchi, A. J., & Werth, C. J. (2015). A hybrid pore-scale and continuum-scale model for solute diffusion, reaction, and biofilm development in porous media. *Water Resources Research*, 51(3), 1846–1859. <https://doi.org/10.1002/2014WR016322>
124. Tareke, E., Rydberg, P., Karlsson, P., Eriksson, S., & Törnqvist, M. (2002). Analysis of Acrylamide, a Carcinogen Formed in Heated Foodstuffs. *Journal of Agricultural and Food Chemistry*, 50(17), 4998–5006. <https://doi.org/10.1021/jf020302f>
125. Teufel, L. W., Rhett, D. W., & Farrell, H. E. (1991). Effect of reservoir depletion and pore pressure drawdown on in situ stress and deformation in the Ekofisk field, North Sea. The 32nd US Symposium on Rock Mechanics (USRMS).
126. Touffet, M., Trystram, G., & Vitrac, O. (2020). Revisiting the mechanisms of oil uptake during deep-frying. *Food and Bioproducts Processing*, 123, 14–30. <https://doi.org/10.1016/j.fbp.2020.06.007>
127. Troncoso, E., & Pedreschi, F. (2009). Modeling water loss and oil uptake during vacuum frying of pre-treated potato slices. *LWT - Food Science and Technology*, 42(6), 1164–1173. <https://doi.org/10.1016/j.lwt.2009.01.008>
128. Troygot, O., Saguy, I. S., & Wallach, R. (2011). Modeling rehydration of porous food materials: I. Determination of characteristic curve from water sorption isotherms. *Journal of Food Engineering*, 105(3), 408–415. <https://doi.org/10.1016/j.jfoodeng.2011.01.027>
129. Vafai, K. (2005). *Handbook of POROUS MEDIA*, Second Edition. CRC Press. <https://doi.org/10.1201/9780415876384>
130. Van As, H., & Van Duynhoven, J. (2013). MRI of plants and foods. *Journal of Magnetic Resonance*, 229, 25–34. <https://doi.org/10.1016/j.jmr.2012.12.019>
131. Van Der Sman, R. G. M., Vergeldt, F. J., Van As, H., Van Dalen, G., Voda, A., & Van Duynhoven, J. P. M. (2014). Multiphysics pore-scale model for the rehydration of porous foods. *Innovative Food Science & Emerging Technologies*, 24, 69–79. <https://doi.org/10.1016/j.ifset.2013.11.008>
132. Vargaftik, N. B. (1975). *Tables on the thermophysical properties of liquids and gases*. Hemisphere Pub. Corp. <https://doi.org/10.1002/aic.690210636>
133. Vauvre, J.-M., Kesteloot, R., Patsioura, A., & Vitrac, O. (2014). Microscopic oil uptake mechanisms in fried products*. *European Journal of Lipid Science and Technology*, 116(6), 741–755. <https://doi.org/10.1002/ejlt.201300278>
134. Vauvre, J.-M., Patsioura, A., Olivier, V., & Kesteloot, R. (2015). Multiscale modeling of oil uptake in fried products. *AIChE Journal*, 61(7), 2329–2353. <https://doi.org/10.1002/aic.14801>
135. Vitrac, O., Trystram, G., & Raoult-Wack, A.-L. (2000). Deep-fat frying of food: Heat and mass transfer, transformations and reactions inside the frying material. *European Journal of Lipid Science and Technology*, 102(8–9), 529–538. [https://doi.org/10.1002/1438-9312\(200009\)102:8/9<529::AID-EJLT529>3.0.CO;2-F](https://doi.org/10.1002/1438-9312(200009)102:8/9<529::AID-EJLT529>3.0.CO;2-F)
136. Wang, N., & Brennan, J. G. (1991). Moisture sorption isotherm characteristics of potatoes at four temperatures. *Journal of Food Engineering*, 14(4), 269–287. [https://doi.org/10.1016/0260-8774\(91\)90018-N](https://doi.org/10.1016/0260-8774(91)90018-N)

137. Weinstein, T. F., Bennethum, L. S., & Cushman, J. H. (2008). Two-Scale, Three-Phase Theory for Swelling Drug Delivery Systems. Part I: Constitutive Theory. *Journal of Pharmaceutical Sciences*, 97(5), 1878–1903. <https://doi.org/10.1002/jps.21208>
138. Whitaker, S. (1999). *The Method of Volume Averaging* (Vol. 13). Springer Netherlands. <https://doi.org/10.1007/978-94-017-3389-2>
139. Xu, T., Zhou, G., Heap, M. J., Yang, S., Konietzky, H., & Baud, P. (2018). The Modeling of Time-Dependent Deformation and Fracturing of Brittle Rocks Under Varying Confining and Pore Pressures. *Rock Mechanics and Rock Engineering*, 51(10), 3241–3263. <https://doi.org/10.1007/s00603-018-1491-4>
140. Yamsaengsung, R., & Moreira, R. (2002). Modeling the transport phenomena and structural changes during deep fat frying: Part I: Model development. *Journal of Food Engineering*, 53(1), 1–10. [https://doi.org/10.1016/S0260-8774\(01\)00134-0](https://doi.org/10.1016/S0260-8774(01)00134-0)
141. Zabransky, M., Ruzicka, V., Majer, V., & Domalski, E. (1997). Heat Capacity of Liquids: Critical Review and Recommended Values-Monograph No. 6. <https://www.nist.gov/publications/heat-capacity-liquids-critical-review-and-recommended-values-monograph-no-6>
142. Zaroni, M. A. B., Wang, J., Torero, J. L., & Gerhard, J. I. (2022). Multiphase modelling of water evaporation and condensation in an air-heated porous medium. *Applied Thermal Engineering*, 212, 118516. <https://doi.org/10.1016/j.applthermaleng.2022.118516>
143. Zhang, J., Datta, A., & Rakesh, V. (2005). Investigation of nonequilibrium in water evaporation, 3rd Inter-American Drying Conference. *Montreal, Canada*.
144. Zhao, B., MacMinn, C. W., Primkulov, B. K., Chen, Y., Valocchi, et al. (2019). Comprehensive comparison of pore-scale models for multiphase flow in porous media. *Proceedings of the National Academy of Sciences*, 116(28), 13799–13806. <https://doi.org/10.1073/pnas.1901619116>
145. Zhao, Y., Kumar, P. K., Sablani, S. S., & Takhar, P. S. (2022). Hybrid mixture theory-based modeling of transport of fluids, species, and heat in food biopolymers subjected to freeze–thaw cycles. *Journal of Food Science*, 87(9), 4082–4106. <https://doi.org/10.1111/1750-3841.16279>
146. Ziaififar, A. M., Achir, N., Courtois, F., Trezzani, I., & Trystram, G. (2008). Review of mechanisms, conditions, and factors involved in the oil uptake phenomenon during the deep-fat frying process. *International Journal of Food Science & Technology*, 43(8), 1410–1423. <https://doi.org/10.1111/j.1365-2621.2007.01664.x>
147. Ziaififar, A. M., Courtois, F., & Trystram, G. (2010). Porosity development and its effect on oil uptake during frying process. *Journal of Food Process Engineering*, 33(2), 191–212. <https://doi.org/10.1111/j.1745-4530.2008.00267.x>
148. Zogzas, N. P., Maroulis, Z. B., & Marinou-Kouris, D. (1994). Densities, shrinkage and porosity of some vegetables during air drying. *Drying Technology*, 12(7), 1653–1666. <https://doi.org/10.1080/07373939408962191>
149. Zuo, H., Yang, Z., Deng, S., & Li, H. (2023). High-order asymptotic solutions for gas transport in heterogeneous media with multiple spatial scales. *Physics of Fluids*, 35(1), 013106. <https://doi.org/10.1063/5.0130971>